

Complementary optical–potential analysis of α -particle elastic scattering and induced reactions at low energies

M. Avrigeanu^{*}, A.C. Obreja, F.L. Roman, V. Avrigeanu

"Horia Hulubei" National Institute for Physics and Nuclear Engineering, P.O. Box MG-6, 76900 Bucharest, Romania

and

W. von Oertzen

Freie Universität Berlin, Fachbereich Physik, Arnimallee 14, 14195 Berlin, and Hahn–Meitner–Institut, Glienicker Strasse 100, 14109 Berlin, Germany

Abstract

A previously derived semi–microscopic analysis based on the Double Folding Model, for α -particle elastic scattering on $A \sim 100$ nuclei at energies below 32 MeV, is extended to medium mass $A \sim 50$ –120 nuclei and energies from ~ 13 to 50 MeV. The energy–dependent phenomenological imaginary part for this semi–microscopic optical model potential was obtained including the dispersive correction to the microscopic real potential, and used within a concurrent phenomenological analysis of the same data basis. A regional parameter set for low–energy α -particles entirely based on elastic–scattering data analysis was also obtained for nuclei within the above–mentioned mass and energy ranges. Then, an ultimate assessment of (α, γ) , (α, n) and (α, p) reaction cross sections concerned target nuclei from ^{45}Sc to ^{118}Sn and incident energies below ~ 12 MeV. The former diffuseness of the real part of optical potential as well as the surface imaginary–potential depth have been found responsible for the actual difficulties in the description of these data, and modified in order to obtain an optical potential which describe equally well both the low energy elastic–scattering and induced–reaction data of α -particles.

Key words: α - ^{50}Ti , ^{51}V , $^{50,52,53}\text{Cr}$, $^{56,58}\text{Fe}$, ^{59}Co , $^{58,60,62,64}\text{Ni}$, ^{63}Cu , ^{89}Y , $^{90,91}\text{Zr}$, $^{92,94}\text{Mo}$, ^{107}Ag , $^{112,116,122,124}\text{Sn}$ optical potentials; Elastic scattering, $E < 50$ MeV; ^{56}Fe , $^{58,62,64}\text{Ni}$, ^{63}Cu , ^{70}Ge , ^{96}Ru , ^{106}Cd , and $^{112,118}\text{Sn}$ (α, γ) , ^{45}Sc , $^{46,48}\text{Ti}$, ^{51}V , ^{50}Cr , ^{55}Mn , ^{54}Fe , ^{59}Co , $^{62,64}\text{Ni}$, $^{63,65}\text{Cu}$, $^{96,98}\text{Ru}$, ^{106}Cd , and ^{118}Sn (α, n) , ^{44}Ti , $^{58,62}\text{Ni}$, ^{96}Ru and ^{112}Sn (α, p) , $E < 12$ MeV; Statistical compound–nucleus reactions
PACS: 21.30.Fe, 21.65.+f, 24.10.Ht, 24.60.Dr, 25.55.Ci, 27.60.+j

Contents

1	Introduction	2
2	The semi-microscopic and phenomenological optical potentials	5
2.1	The Double-Folding real potential	5
2.2	The semi-microscopic and phenomenological optical potentials	6
3	(α, α) semi-microscopic and phenomenological analysis	7
4	(α, x) and total α -reaction cross section analysis	10
4.1	Particular ROP features below the Coulomb barrier	10
4.2	Effects within the whole energy range of ROP particular amendment below the Coulomb barrier	12
4.3	$A \leq 54$ target nuclei	13
4.4	$A \sim 63$ target nuclei	14
4.5	$A \geq 100$ target nuclei	15
5	Conclusions	16
	References	17

1 Introduction

The α -nucleus optical model potential (OMP) plays a key role in studies of nuclear structure and nuclear reactions, e.g. it is used to unify the bound and scattering α -particle states [1], to analyze the superheavy nuclei α -decay half-lives [2], in basic nuclear astrophysics applications [3] and for the estimation of radiation-damage effects in fusion test facilities and accelerator-driven systems. A successful global optical potential was formerly obtained by Nolte et al. [4] only for α -particle energies above 80 MeV. At the same time, it has already been observed that the results obtained from the analysis of the low-energy elastic scattering data suffer from discrete and continuous ambiguities in the OMP parameters. Moreover, two main questions are still open: (i) the OMP parameter sets obtained from α -particle elastic scattering at high energies [4] do not describe either the lower-energy (< 40 MeV) elastic scattering or

* Corresponding author. Tel.: +40-21-4042300
Email address: mavrig@ifin.nipne.ro (M. Avrigeanu).

the complete fusion data, and (ii) the statistical α -particle emission is underestimated by the OMPs that account for elastic scattering on the ground-state nuclei [5,6,7,8]. In the latter case, the need for new physics in potentials to describe nuclear de-excitation within the statistical model calculations has already been pointed out [9]. Similarly, the effects caused by changes of the nuclear density at a finite temperature have been considered in this respect within the real part of the double folding model (DFM) of the alpha-nucleus optical potential [10].

Three improved semi-microscopic global optical potentials have been derived recently [11] in order to reproduce α -particle elastic scattering as well as α -induced and (n, α) reaction data, by using the same DF real potential and WS imaginary parts with either a purely volume imaginary term (I), or a volume plus surface imaginary potential (II), as well as a damped surface potential together with the dispersive contribution to the real DF potential (III). In spite of these quite distinct assumptions, it has been shown that these three OMPs lead to cross sections which do not exhibit any substantial differences apart for some cases at backward angles. However, all three of them show an uncertainty factor of 10 up to which it has been possible to predict globally α -induced reaction cross sections [11]. As a result, in order to avoid any question concerning the remaining parameters largely needed within statistical model calculations, a DFM-based semi-microscopic analysis of only α -particle elastic scattering on $A \sim 100$ nuclei at energies from ~ 14 to 32 MeV has been carried out [12]. The use of this potential at even lower energies has provided a suitable description of the (α, n) reaction cross sections for lighter target nuclei with $A \leq 54$ [13], while it has led to a major overestimation of (α, γ) reaction cross sections for ^{106}Cd [14] and ^{112}Sn [15]. Better results have been provided in the later cases by either the well-known mass- and energy-independent four-parameter global potential of McFadden and Satchler [16] obtained by analysis of 26 MeV α -particle elastic scattering, or with the potential of Refs. [17,18] which was fitted to (n, α) and (α, γ) reaction data around $A \sim 145$. At the same time the measured (α, n) and (α, p) reaction cross sections [14] have been described only by the OMPs of Refs. [10,16] while even the α -potential of Galaviz et al. [19], which was deduced from the α -particle elastic scattering on ^{112}Sn at energies close to the Coulomb barrier, only poorly describes the data for α -capture on ^{112}Sn at energies lower than 2–6 MeV. A common final assumption [14,15], related to a similar overestimation of the (α, γ) data and an underestimation of the (α, p) data, has been that these deviations are not only caused by the α -potential. However, the quotation in Ref. [14] of Ref. [10] for the possible difference between optical potential derived from scattering and reaction data, discarded the distinction between the incident and the emitted α -particles discussed within the latter paper. One may indeed keep in mind the difference in energy range within which an α -particle potential is usually established by analysis of the elastic scattering, and that of the α -induced reactions of astrophysical interest. Similar questions have been raised

by a rather recent analysis for the target nuclei ^{63}Cu [20], $^{96,98}\text{Ru}$ [21] and ^{118}Sn [22].

A global α -nucleus optical potential has been proposed by the BARC group [23] for $A \sim 12$ –209 and energies from the Coulomb barrier up to about 140 MeV, based on the systematics of the real and imaginary potential volume integrals established by Atzrott et al. [24] by using a DFM real part and the description in a unified way of elastic scattering data for $A=40$ –208 and energies from 30 to 150 MeV, as well as bound state properties. The BARC global potential has been found to describe well the high energy elastic-scattering data, while at lower energies the calculations and the data differ considerably and further investigation has been found necessary [23]. Next, an acceptable quality of fits has been considered for the calculation of nuclear reactions with α -particles especially in the entrance channel. However, this conclusion could be influenced, at very low incident energies, by the comparison with the results obtained by using improperly the distinct OMP for emission of α -particles [8].

The recent high precision measurements of α -particle elastic-scattering, e.g. [19,25,26], pointed to additional features of the α -particles scattering at low energy. Consequently, further eventual improvement of global OMP parameters obtained previously through semi-microscopic analysis of the low-energy α -particle elastic scattering become possible [27]. It is discussed in the present work with reference to the mass region $50 \leq A \leq 124$ and energies below 50 MeV. Following the above-mentioned studies which aim to describe both the α -particle elastic scattering and reaction data, we have first attempted to understand the failure of α -particle OMPs from elastic-scattering analysis, to describe the reaction data. Thus, getting an insight on moving below the Coulomb barrier from the energy range where the α -particle OMPs are usually established by elastic-scattering analysis, the eventual difference of α -particle potentials in the entrance/exit channels [8,10] could be made clear.

The present work aims firstly to extend the previous semi-microscopic analysis of Ref. [12] on lighter nuclei ($A \sim 60$) in order to use the corresponding larger data basis of the α -particle elastic scattering. The basic model ingredients are given in Sec. 2 while the results of the semi-microscopic analysis of the experimental α -particle elastic scattering on $A < 124$ nuclei at energies below 50 MeV, performed in order to adopt a proper energy-dependent phenomenological imaginary part, are described in Sec. 3. The work is completed by a full phenomenological analysis of the same data, leading to a regional optical potential (ROP) parameter set. Its connection to a survey of α -particle induced reaction data below 12 MeV is given in Sec. 4, starting with the accurate total-reaction cross sections of Vonach et al. [28] and including the open questions recently noted for ^{63}Cu [20] and $A \sim 100$ nuclei [14,15,21,22]. As a matter of fact, in order to calculate the reaction cross section we have used a consistent parameter set established by analyzing various independent exper-

imental data for all stable isotopes of V, Mn, Co, Ni, Cu [29,30,31], Mo [32], Pd, Sn and Te [33]. Thus, it became possible to focus on the uncertainties of the α -particle OMP parameters and their improvement. Final conclusions are provided in Sec. 5. Preliminary results have been presented elsewhere [13,34].

2 The semi-microscopic and phenomenological optical potentials

2.1 The Double-Folding real potential

Various attempts have been made to replace the phenomenological real potential of Woods-Saxon (WS) type by a microscopic α -nucleus potential using an effective nucleon-nucleon (NN) interaction, in order to avoid too much phenomenology in the description of the α -particle elastic scattering data. Actually the DF method [35], with an effective NN -interaction folded with the mass distributions of both the target nucleus and the projectile, has been widely used to generate OMPs for nucleons, α -particles and heavy-ions (e.g., [35,36,37]). The M3Y-Reid [38] and Paris [39] are the most familiar interactions [35,36,40], while a density dependence of the NN -interaction has been also incorporated [37,41,42]. However, the M3Y-interactions can be used only to obtain the real potential, and the imaginary term must be parameterized independently (e.g. [40]) or simply taken from a phenomenological OMP [35]. As a first result, the former approach may reduce the number of the OMP parameters and corresponding uncertainties, its success being proved in the description of the elastic scattering of many systems [40].

More recently the DF formalism for the α -nucleus optical potential has been revised at α -particle energies above 80 MeV, in order to study the exchange effects and density dependence of the effective NN -interaction [37]. However, the situation is considered less clear for the α -nucleus OMP at low energies, where the imaginary-potential is strongly energy dependent and nuclear structure effects should be taken into account, the data being mainly sensitive to the potential at the nuclear surface. Therefore, in addition to the results of Khoa [37], suitable constraints for OMP parameters at α -particle energies around the Coulomb barrier have been checked [12] using the most advanced DFM version with the explicit treatment of the exchange component and no adjustable parameter or normalization constant.

The key ingredients of the DFM calculations which are the effective NN -interaction and the nuclear-density distributions of the interacting nuclei, have been enlightened by the analysis [12] of the α - α elastic-scattering angular distributions measured at incident energies below the reaction threshold of 34.7 MeV for the first open channel ${}^7\text{Li} + \text{p}$. These data were found to

be better described by the M3Y–Reid [38] than by the M3Y–Paris [39] effective NN –interaction, both folded with the Baye et al. [43] α –particle density distribution. This choice provides a better agreement with the data as compared to the Satchler–Love [35] and Tanihata et al. [44] forms. Moreover, the density dependence of the M3Y effective NN –interaction, which accounts for the reduction of the interaction strength with increasing density was chosen with a linear energy dependence (BDM3Y type) [41] provided by the analysis [12] of angular distributions of the elastically scattered α –particles on ^{90}Zr at energies between 21 and 25 MeV.

Finally, the nuclear density distribution of the target nuclei needed in the DFM has been described by means of a two–parameter Fermi–type function with the parameters chosen to reproduce the electron scattering data [45,46] and the shell model calculations [47]. The basic formulas for the calculations of the DFM real part of the optical potential as well as the rest of the model assumptions are given in Ref. [12].

2.2 *The semi–microscopic and phenomenological optical potentials*

Similarly to the semi–microscopic analysis in Ref. [12] of the α –particle elastic scattering on $A \sim 100$ nuclei, at energies below 32 MeV, we obtained the energy–dependent phenomenological imaginary potential using the corresponding dispersive correction $\Delta U(r, E)$ to the microscopic ”parameter free” DF real potential $U_{DF}(r, E)$ within the complex optical potential $U(r)$,

$$U(r) = V_C(r) + U_{DF}(r, E) + \Delta U(r, E) + iW_V f(r, R_V, a_V) + iW_D g(r, R_D, a_D). \quad (1)$$

The same volume (V) and surface (D) imaginary potentials have then been involved within a phenomenological analysis of the same data basis, leading to a ROP with Woods–Saxon (WS) form factors for both real and imaginary parts:

$$U(r) = V_C(r) + V_R f(r, R_R, a_R) + iW_V f(r, R_V, a_V) + iW_D g(r, R_D, a_D), \quad (2)$$

where $f(r, R_i, a_i) = (1 + \exp[(r - R_i)/a_i])^{-1}$, $g(r, R_i, a_i) = -4a_i d/dr [f(r, R_i, a_i)]$, and $R_i = r_i A^{1/3}$, A being the target–nucleus mass number. $V_C(r)$ is the Coulomb potential of a uniformly charged sphere of radius R_C while $r_C = 1.30$ fm. The additional surface term of the imaginary part, with the derivative shape, has been introduced at lower energies because of the importance of direct reactions, while the number of direct channels is still small in this energy range.

W_D decreases with increasing energy and vanishes at few tens of MeV, e.g. Refs. [11,25,48].

It should be emphasized that no adjustable parameter or normalization constant has been involved within this analysis for the real part of Eq. (1) in order to determine the imaginary part of the OMP, so that the predictive power of this semi-microscopic potential is preserved. On the other hand, the widely used renormalization factor [37] for the real semi-microscopic potential is a convenient way to take into account the absorption from the elastic channel and the presence of couplings to other channels [49,50], while these effects can be represented by the imaginary-potential dispersive contribution to the total real potential in addition to the real DF potential [51,52,53]. The analytical solution for the dispersion relation [51] adopted and discussed previously [12] has been used also in the present work.

3 (α,α) semi-microscopic and phenomenological analysis

Since the previously published phenomenological analyses of α -particle elastic scattering data for $50 \leq A \leq 124$ target nuclei were performed for various target nuclei only at specific incident energies, and the systematic behavior of the mass or energy dependences of the corresponding OMP parameters were not considered, we have looked for a consistent parameter set able to describe the bulk of these data at lower, e.g. ≤ 50 MeV, incident energies. Thus we have analyzed experimental angular distributions of α -particle elastic-scattering on target nuclei from ^{50}Ti to ^{124}Sn and α -particle energies from 8.1 to 49 MeV (see Table 1, where an overview on the present data and results of the analysis is given).

Within our two-step OMP approach [12], we determined first the parameters of an energy-dependent phenomenological imaginary part while the parameter-free DF potential, Eq. (1) was used for the OMP real part. The computer code SCAT2 [70] has been used, modified to include the semi-microscopic DF potential of Refs. [41] as an option for the real potential. Unfortunately an analysis of the χ^2 -deviation per degree of freedom between the experimental and calculated cross sections, which would have been the optimal procedure, has not been possible in all cases due to the lack of numerical cross-sections including the corresponding errors for some of the experimental data given in Table 1. Nevertheless, this procedure was applied for the more recent data using the original errors and a good overall agreement was obtained for various target nuclei, thus providing a suitable validation of the actual OMP parameter sets.

In order to have the usual WS-parameterizations according to Eq. (2), phe-

nomenological analysis of the same data was then carried out keeping the imaginary part unchanged from the former semi-microscopic analysis. In fact, minor adjustment were involved for the imaginary potential depths (Table 2) but none for the related average geometry parameters given in Table 3. The advantage of having already well settled about half of the usual OMP parameters increases obviously the accuracy of the local fit of data (Figs. 1–7). This procedure reduces to a great extent the problem of OMP continuous ambiguities in the real potentials of WS shape, as noted previously also by Mohr et al. [71]. However, the question of discrete ambiguities known as the "family problem", with various real potential depths V_R leading to comparable fits to the experimental data as shown in Fig. 8 is still open. The similar χ^2 minima have been obtained by continuous variation of the V_R value and readjusting correspondingly the real-potential geometry parameters. For the last two quantities continuous ambiguities within the same discrete ambiguity (as, e.g., in Fig. 1 of Ref. [16]) are not shown but the values corresponding to the optimum values of V_R , in order to point out the trend of their change with "families". As a matter of fact, the origin of the discrete ambiguity has been well understood from the beginning as different numbers of half-wavelengths are included within the potential well [16], while the elastic scattering analysis alone is not able to solve this problem [72]. However, Mohr et al. [71] have shown that, once very accurately measured scattering data became available, one may discriminate between discrete values of the real-potential volume integrals per interacting nucleon pair, given by the general form

$$J_x(E) = \frac{1}{A_1 A_2} \int U_x(r, E) d^3r. \quad (3)$$

where $x=R, V, D$. Thus we have looked also for the J_R values corresponding to the χ^2 minima in Fig. 8 as well as for all angular distributions analyzed in the present work (Table 2). As a result, most of these minima are related to values of about $J_R \sim 380\text{--}440 \text{ MeV fm}^3$, around the α -particle energy of 25 MeV (Fig. 1), slightly decreasing with energy. Therefore these best-fit WS real-potential parameters have been selected in the cases where more similar χ^2 minima exist, and involved subsequently in a procedure of deriving average mass-, charge-, and energy-dependent parameters for the mass and energy ranges of this work, but as close as possible to those introduced by Nolte et al. [4] above 80 MeV. Since it is well-known [16], that a linear interpolation between the optimum values does not lead to parameter values which describe the data reasonably well, the dotted curves in Fig. 8 having only the role to display a trend, these average dependences were not obtained at once for all real potential parameters. In order to reduce as much as possible the adverse effects of the averaging, the fit of the data was repeated each time after the average dependences were derived, and the result consequently used first for the reduced radius and afterward for the potential depth. The local a_R values obtained finally by using average values for the rest of all OMP parameters are

shown in Fig. 9 versus the α -particle energy as well as for ratio to the Coulomb barrier value. The mass dependence of the values of the interaction radius R_B [73] used in this respect, given in Table 3, emphasizes a similar importance of energy- and mass-dependences of the real-potential diffuseness, appropriately described by the form given in Table 3 for energies from the Coulomb barrier to ~ 25 MeV. However, the spread of these local parameter values at higher energies has not been fully understood, so that an average value of $a_R=0.55$ fm has been adopted for the energy range above a value E_3 given in Table 3.

While the real J_R , volume J_V and surface J_D imaginary components of the local phenomenological potentials are also given in Table 2, the J_R values corresponding to the average OMP parameters of Table 3 decrease from ~ 410 to ~ 370 MeV fm³ between the α -particle energies ~ 12 –50 MeV. These values correspond to volume integrals between ~ 310 –280 MeVfm³ for the microscopic DFM potentials which provide a similar description to the elastic scattering data at low energies, and being almost identical in the tail region (e.g., Fig. 10 of Ref. [12]). Actually, the differences between these volume integrals of microscopic DF and phenomenological real potentials are simply due to their different radial dependence, which should be taken into account when the two types of potentials are compared. Therefore we have once more found [12] that our J_R values correspond to microscopic DFM volume integrals which are 10% lower than expected from the systematics found in [19,24,25,71,74]. They are also similar to those obtained by using the semi-microscopic potential III of Ref. [11] at the same energies, or derived from the analysis of α -decay [2,74].

The angular distributions calculated using these average parameters (regional optical potential – ROP) are shown in Figs. 1–7, in order to emphasize its usefulness and related deviations from the local analysis results. Moreover, the predictions of the most recent global parameter set of Kumar et al. [23] are included, while those provided by McFadden and Satchler with a four-parameter global potential [16] have already been presented elsewhere [13]. A comparison of semi-microscopically calculated angular distributions and ROP results is shown in Fig. 10(a) for the lowest α -particle energies on ⁵⁸Ni, within a discussion to be given in Section 4.2 on the effects of a ROP particular amendment below the Coulomb barrier. On the whole, a really improved description of the data is provided by the present ROP. Moreover, it should be noted that a rather suitable account of the data is also obtained using OMPs with real-potential diffuseness a_R [12,16] notably lower than the a_R values which are needed in order to describe α -particle emission from excited compound nuclei [8,10].

4 (α, x) and total α -reaction cross section analysis

4.1 Particular ROP features below the Coulomb barrier

The enlarged analysis of the α -particle optical potential based on the elastic scattering data, achieved mainly at energies above the Coulomb barrier, makes one confident to check its suitability at even lower energies. Actually one may expect that a simple extension of the corresponding OMP parameters, below the energies involved within their establishment, could be reliable provided that these parameters vary regularly over the entire energy range. For the α -particle energies below the Coulomb barriers this could be the case of, e.g., the real and volume imaginary potential but not for the surface imaginary potential according to the related comment in Sec. 2.2. The analysis of the (α, x) reaction cross sections below the Coulomb barrier may reveal OMP parameters different by those at the former energies. On the other hand, a change of the surface imaginary potential depth below the Coulomb barrier is related indeed to a variation of the corresponding dispersive correction (inset in Fig. 10) to the real part of the semi-microscopic potential, so that an additional analysis should concern the eventual effects on the first step of our ROP setting up.

First, we have used the ROP parameters given in Table 3 for energies above the Coulomb barrier, for Hauser-Feshbach statistical model calculations of (α, x) reaction cross sections. They were carried out similarly to the previous analysis of (n, α) reaction cross section for $A \sim 90$ [10,75], except the investigated OMP was now related to α -particles in the incident channel. For the rest of statistical-model parameters we have used consistent sets established by analyzing various independent experimental data for all stable isotopes of V, Mn, Co, Ni, Cu [29,30,31], Mo [32], and Pd, Sn and Te [33]. While a suitable description of the (α, n) reaction cross sections was found for lighter target nuclei with $A \leq 54$ (Fig. 11), well improved over the $\sim 10\%$ accuracy [13] provided by the global parameter sets of McFadden and Satchler [16], a major overestimation of (α, γ) reaction cross sections resulted for the target nuclei $^{62,64}\text{Ni}$ (Fig. 12), ^{63}Cu (Fig. 13), $^{96,98}\text{Ru}$ (Fig. 14), and ^{106}Cd and $^{112,118}\text{Sn}$ (Fig. 15). For this latter class of nuclei, definitely marked by larger charge and atomic numbers, even the global OMP of McFadden and Satchler provided better results [14,15,20,21] than our former ROP based on elastic-scattering data analysis [12]. On the other hand, the calculated reaction cross sections corresponding to this global potential vary with respect to the experimental data, from an underestimation around 10% for target nuclei with $A \sim 60$ [13] to much larger overestimation for $A > 100$ [14,15]. Therefore, in order to understand better the behavior of these reaction data, we chose to analyze them against the ratio $E_{c.m.}/B_C$ between the incident energy in the

center-of-mass system and the Coulomb barrier (Figs. 11–15). The total α -reaction cross sections provided only by the ROP parameters established by the elastic-scattering analysis alone are additionally shown in Figs. 12–15 for the target nuclei with $A > 60$. The energy ranges within which the (α, γ) and subsequently (α, n) reactions control the whole α -particle interaction by the α -particle OMP become thus obvious.

A major source of uncertainty has been the real-potential diffuseness a_R , which is the OMP parameter marked by the largest sensitivity of statistical-model calculated cross sections (e.g., Ref. [10]). The systematics provided by the analysis of the elastic-scattering data for $E_{c.m.}/B_C > 0.9$ (Fig. 9) imply a real-potential diffuseness increasing with the energy decrease, confirmation of this behavior being essential since a similar trend is specific to OMP describing the α -particle emission [8,10]. Its establishment at very low energies would therefore override any additional assumption related to different OMP parameter sets in the incident and emergent channels, respectively. However, the account of measured (α, x) reaction cross sections seems to presume a decrease of this parameter with the energy decrease. Thus, with no other data at hand, a constant a_R value appears as the foremost option for the real-potential diffuseness at energies lower than a value, E_2 , corresponding to $0.9B_C$ (Table 3). A second run of statistical-model calculations using this assumption shown by dashed curves for some of the reactions in Figs. 12–15 provides calculated cross sections lower than the former ones by less than 10% for $A \sim 60$ (Fig. 12) and $\sim 15\%$ for $A > 100$ (Fig. 15). This minor change proves that a constant a_R below the Coulomb barrier, being yet an appropriate choice within the actual knowledge, can not account for the low energy (α, x) reaction data.

Since the real and volume imaginary potential are less uncertain, as noted in the beginning of this section, the surface imaginary potential remains the central point of discussion. Actually Mohr et al. [71] pointed out that the strong change of the number of open reaction channels close to the Coulomb barrier leads to a strong variation of the surface and volume imaginary potentials. This variation has been described by a parametrization of the imaginary-potential volume integral either according [24,71] to Brown and Rho [76] or by using a Fermi-type function [11,25,77]. On the other hand it has been pointed out [19,25] that the actual ambiguities do not allow to determine the shape of the imaginary potential and reduce the reliability of extrapolations to lower energies. Therefore, our final change of the ROP obtained by elastic-scattering analysis, in order to describe the (α, x) reaction data at these energies, has been the drop of the surface imaginary potential depth with the decrease of α -particle energy below the energy limit E_2 . This choice is consistent with the above-mentioned strong change of the number of open reaction channels close to the Coulomb barrier, tightly matched by the E_2 values with the mass dependence shown in Fig. 16. Following this consideration and the demand of suitable description of the excitation functions in Figs. 12–15, we have ob-

tained the corresponding slope of the $W_D(E)$ energy-dependence in Table 3. Its average value of 6 would then determine the starting point E_1 of the surface imaginary-potential energy range. However, in order to avoid overall numerical problems just above reaction thresholds, we have not finally chosen a vanishing value of the potential depth W_D at the very low energy but a minimum value of 4 MeV. This depth limit and aforementioned slope of the $W_D(E)$ eventually lead to the E_1 global expression given in Table 3 for the final form of ROP in the whole energy range below 50 MeV. Other E_1 values, related to a constant value of W_D lower than 4 MeV at the null α -particle energy, may even provide an improved agreement with the measured data in particular cases mentioned in the following. Moreover, one can now explain the poorer results for (α, x) reaction data of the former α -particle ROP based on the elastic-scattering analysis alone [12] as compared to the four-parameter global potential [16] and related OMPs [17,18] which have only a volume imaginary potential with a constant depth. As a result, the lack of an energy-decreasing surface component has prevented larger deficiencies in the fits which arise in extrapolations below the Coulomb barrier.

4.2 Effects within the whole energy range of ROP particular amendment below the Coulomb barrier

The latest change of the surface imaginary potential depth below the Coulomb barrier should be followed by a corresponding change, through the dispersive relations with an integral over all incident energies, in the real part of the semi-microscopic potential which has been the first step of our ROP setting up. Therefore, one may consider that the iterative procedure applied in order to find the best description of the elastic-scattering data should be resumed by using the modified surface imaginary potential depth within the dispersive correction formula, e.g., Eq. (4.2) of Ref. [12]. The corresponding correction to the DF real potential for the target nucleus ^{58}Ni , due to only the final form of the ROP surface imaginary-potential (Table 3), is shown within the inset in Fig. 10(a) while the rest of the matching discussion is as for Fig. 4 of Ref. [12]. This correction is compared with the former curve, obtained by using the analytical solution and forms adopted previously [12,27], as mentioned in Sec. 3.2. The only change in this respect concerned, following the trend of the local parameter values found in this work as well as the lack of data below α -particle energy of ~ 9 MeV, a constant increasing surface imaginary potential depth between the axes origin and the corresponding prediction in Table 3 at the latter energy. It results that the difference between the former and final values of this particular dispersive correction is well decreasing below 2 MeV for energies increasing above ~ 15 MeV. This quantity is however quite low with respect to the real potential depths around 50 MeV within the nuclear surface region, where this correction is effective. At the same time, if this change would

be involved in a new iteration of the first step of our ROP setting up, for the the imaginary potential parameters, it is obvious that the consequent changes of these potential depths would be comparable to the minor adjustment of the same depths mentioned in Sec. 3, carried out within the second step of our approach. Larger changes of ≤ 5 MeV for the dispersive correction due to the surface–imaginary potential variation below the Coulomb barrier are present only in the case of the elastic–scattering data on ^{58}Ni between 8 and ~ 10 MeV. Nevertheless, it would be less effective also at these energies to look for imaginary–potential parameters within a new iteration of the semi–microscopic analysis of elastic–scattering data, due to the already very low sensitivity of the calculated elastic–scattering cross sections to the imaginary potential. Thus, except some obvious limits, the corresponding χ^2 minima are so slowly varying with the imaginary potential depths that no real change of these parameters may result. Alternatively, we have chosen to compare in Fig. 10(a) the semi–microscopical elastic–scattering cross sections on ^{58}Ni at these low energies calculated by using the same local imaginary–potential parameters (Table 2) but the different former and final dispersive corrections shown in the inset as well. Even these effects are small and obviously within the experimental data bars.

Another point which had to be made clear was the consequence of the change itself of ROP parameters a_R and W_D due to the (α, x) reaction cross section analysis, on the formerly calculated angular distributions of α -particle elastic–scattering by using the parameter forms established for energies higher than E_2 (Table 3). This again has been the case of only the elastic–scattering data on ^{58}Ni between 8 and ~ 10 MeV, shown in Fig. 10(b) to have very similar description before and after the above–mentioned changes of the a_R and W_D parameter forms. It should be noted once more that this status follows the low variation of these parameters at energies rather close to the E_2 limit, as well as the minor sensitivity to the imaginary potential of the corresponding elastic–scattering cross sections dominated by the Rutherford component. Hence we may conclude that the changes of the ROP parameters below the Coulomb barrier have effects already within uncertainties of the parameter values in the rest of the energy range, so that the ROP parameters in Table 3 describe equally well both the elastic–scattering and induced–reaction data of α -particles.

4.3 $A \leq 54$ target nuclei

The particularly accurate (α, n) and total α -reaction cross sections for ^{48}Ti and ^{51}V measured and respectively established by Vonach et al. [28], obviously overestimated by the α -particle emission OMP [8], are slightly better described by the final ROP than by its former version obtained through the

analysis of the elastic-scattering data alone (Fig. 11). The same has been proved [13] to be true also for an enlarged systematics [78,79,80,81,82,85,86] discussed recently [23], and several data sets [83,87] lastly taken into account. The related incident-energy range can hardly explain the difference with respect to the same comparison just above $A=60$ (Fig. 12). The reference to the Coulomb barrier values, so close to the edge E_2 (Fig. 16) between the two distinct energy regions of the present ROP (Table 3), is ultimately making the point clear. The energies concerning these target nuclei are mainly above and around the Coulomb barrier, while in the rest of cases they are clearly below it. The two calculated functions for each reaction are indeed plainly different only for $E_{c.m.}/B_C < 0.9$, while their variance is less visible along the steep part of the excitation functions.

4.4 $A \sim 63$ target nuclei

The data for the target nuclei $^{58,62,64}\text{Ni}$ [80,89,90,91] have been important for the aims of the present work since they illustrate the cross-sections trend for nearby isotopes of the same element and the (α, γ) as well as (α, n) and (α, p) reactions, which represent the total α -reaction cross section in the former and latter halves of the energy range concerned, respectively (Fig. 12). Actually only the data for the $^{62,64}\text{Ni}$ target nuclei [91] were formerly involved in the analysis leading to the final ROP parameters (Table 3), which were consequently applied within the cross-section calculation for ^{55}Mn [88] and ^{58}Ni . On the other hand, the best description has been obtained for the smoother data in the latter case, due to the related energy range and Q-effects, while less accurate results were obtained for the heavier isotopes in Fig. 12. Fortunately, this was not the case of the more recent data [20] for the $^{63}\text{Cu}(\alpha, \gamma)^{67}\text{Ga}$ reaction. The odd proton-numbers of the target and the compound and residual nuclei, with larger nuclear level densities, make the statistical-model calculations more reliable. The appropriateness of the last comment is also proved by the agreement of the calculated and experimental cross sections, although the same consistent parameter set [30,31] has been involved for all four target nuclei.

A similar case but due to a distinct reason occurs for cross sections of the (α, γ) reaction on ^{56}Fe and ^{70}Ge obtained as well as for (α, n) reaction (Fig. 13) by using straightforwardly the final ROP. While the energy range of the existing (α, n) reaction data was as large as for nuclei with $A \leq 54$ with respect to the Coulomb barrier, that of the (α, γ) reaction was again quite narrow. However, the corresponding cross sections have been very close to the total reaction cross sections over at least the former half of this energy range. It results thus a larger sensitivity of the model calculations to the α -particle OMP parameters, in comparison with that of the (α, n) reaction analysis for

similar nuclei also shown in Fig. 13. Nevertheless, a very good agreement with the measured data has been achieved for both reactions. Altogether, the analysis for Ni and Cu isotopes has validated the ROP predictions for the total α -reaction cross section over more than four orders of magnitude.

4.5 $A \geq 100$ target nuclei

The simultaneous measurements of the (α, γ) , (α, p) , and (α, n) reaction cross sections on the target nuclei ^{96}Ru [21] and ^{106}Cd [14] provide the most useful support for the α -particle OMP discussion at the lowest energies below the Coulomb barrier. The measured data of the first two of these reactions on the target nucleus ^{112}Sn [15] have rather similar conditions, while the related neutron emission threshold is much higher in energy. The simultaneous description of these data is most important for the validation of α -particle OMP below the Coulomb barrier, especially within the energy ranges where the (α, γ) and subsequently (α, n) reactions stand for nearly the whole range of the α -particle interaction. On the other hand, the assumption [14,15] concerning the similar overestimation of the (α, γ) cross sections and underestimation of the (α, p) cross sections, caused not only by the α -potential, led us to an additional investigation in this respect [33]. Thus, we analyzed the neutron total cross sections for the Cd, Sn and Te isotopes and the neutron energies up to 30 MeV, as well as the neutron capture on the same target nuclei for the neutron energies up to 3 MeV. A better knowledge of the neutron OMP and then of the γ -ray strength functions has been therefore obtained and applied within the present study of the (α, x) reaction cross sections.

First, we can state, that the calculated cross sections for the (α, γ) reaction on ^{96}Ru (Fig. 14), ^{106}Cd and ^{112}Sn (Fig. 15) are in good agreement with the measured data, especially at α -particle energies where this reaction stands for nearly the whole range of the α -particle interaction. An even better description of these data could be obtained with small adjustments of the ROP parameters a_R and W_D , since our main interest is to obtain a general account of more experimental data using the same parameter set. The results are less satisfactory for the target nucleus ^{118}Sn (Fig. 15). However, this happens at α -particle energies where the (α, γ) reaction cross sections are at least one order of magnitude smaller than the total α -reaction cross sections which go mainly in the (α, n) reaction channel.

Secondly, the cross sections of the concurrent reactions (α, p) , and (α, n) on ^{106}Cd are quite well reproduced, as well as the (α, p) reaction on ^{112}Sn (Fig. 15). A particular case is that of the target nucleus ^{96}Ru at the α -particle energies around the threshold where the neutron emission becomes possible and increases very rapidly, at the expense of the (α, p) reaction cross sec-

tions. Since this effect is observed similarly to the (α, n) reaction on ^{98}Ru (Fig. 14), one may consider this model–calculation failure to be the result of a less suitable account of the neutron and proton emission channels. This observation also explains the approximately correct reproduction of the slope of the $^{118}\text{Sn}(\alpha, \gamma)^{121}\text{Te}$ excitation function. Nevertheless, the comparison of the calculated and measured (α, γ) reaction cross sections at energies where they represent the total α –reaction cross sections gives a good validation of the α –particle ROP.

5 Conclusions

The analysis of the α –particle elastic scattering on $50 \leq A \leq 124$ nuclei at energies below 50 MeV has been carried out using the semi–microscopic DF approach. The energy–dependent phenomenological OMP imaginary part, which was obtained in this case, using the dispersive correction to the DF real potential, has been then used for a completely phenomenological analysis of the same data basis. By using the real DF potential and adjusting only the imaginary OMP part parameters, the number of free parameters are well decreased. Afterward, we adjusted only the parameters of the real phenomenological potential of Woods–Saxon shape while the imaginary components remained unchanged. An average of the local parameter values has been obtained in order to provide finally a regional parameter set which can be easily used in further analyses or predictions.

Moreover, the ROP obtained in the present work has been applied in the statistical–model analysis of the (α, x) reaction cross sections below the Coulomb barrier available below 10–12 MeV for nuclei within the same mass range. For the rest of statistical–model parameters we have used consistent sets established by analyzing various independent experimental data for all stable isotopes of V, Mn, Co, Ni, Cu [29,30,31], Mo [32], and Pd, Sn and Te [33], which finally allow us to focus on the uncertainties of the α –particle OMP. While a suitable description of the (α, n) reaction cross sections was found for lighter target nuclei with $A \leq 54$, a major overestimation of (α, γ) reaction cross sections resulted for $^{62,64}\text{Ni}$, ^{63}Cu , $^{96,98}\text{Ru}$, ^{106}Cd and $^{112,118}\text{Sn}$. This behavior is related to the energies above and around the Coulomb barrier, for the former mass range, and clearly below it for the latter. A suitable description of the (α, x) reaction data below the Coulomb barrier is no longer possible by means of the optical potential provided by the elastic–scattering data analysis above this barrier, a modified surface imaginary potential being necessary. A reliable assessment of the final ROP below the Coulomb barrier has been given by its straightforward and successful use in calculations of reaction cross sections for the target nuclei ^{44}Ti , ^{55}Mn , ^{56}Fe , ^{59}Co , ^{58}Ni , ^{65}Cu , and ^{70}Ge .

Actually, the drop of the surface imaginary potential depth with the decrease of α -particle energy below the Coulomb barrier, necessary for the (α, x) reaction data account, is in line with the strong change of the number of open reaction channels within this energy range. It can also explain the even worse results of the former α -particle ROP based on the elastic-scattering analysis alone [12], when used in the (α, x) reaction data analysis, as opposed to the four-parameter global potential [16] and related OMPs [17,18] which have only a volume imaginary potential with a constant depth. The lack of an energy-dependent surface component thus prevents larger negative effects by extrapolation below the Coulomb barrier. On the other hand, becoming aware of the changes of α -particle OMPs obtained through elastic-scattering analysis alone, in order to describe the (α, x) reaction-data as well, the difference between the α -particle OMPs in the entrance and exit channels could be easier understood. Thus, the present insight into the behavior of the α -particle optical potential at very low incident energies will make possible a further concluding assessment of the α -particle emission at similar energies but in the exit channels [8,10].

Acknowledgments

This work was supported in part by the EURATOM-MEdC Fusion Association, the Research Contract No. 12422 of the International Atomic Energy Agency, and MEdC (Bucharest) Contract No. CEEEX-05-D10-48.

References

- [1] P.E. Hodgson, *Contemp. Phys.* 31 (1990) 99; 31 (1990) 295.
- [2] P. Mohr, *Phys. Rev. C* 73 (2006) 031301; V. Yu. Denisov, H. Ikezoe, *Phys. Rev. C* 72 (2005) 064613.
- [3] M. Arnould, S. Goriely, K. Takahashi, *Phys. Rep.* 450 (2007) 97.
- [4] M. Nolte, H. Machner, J. Bojowals, *Phys. Rev. C* 36 (1987) 1312.
- [5] L.W. Put, A.M.J. Paans, *Phys. Lett. B* 49 (1974) 266; *Nucl. Phys. A* 291 (1977) 93.
- [6] P.P. Singh, P. Schwandt, *Nukleonika* 21 (1976) 451.
- [7] J.M. Alexander, M.T. Magda, S. Landowne, *Phys. Rev. C* 42 (1990) 1092.
- [8] V. Avrigeanu, P.E. Hodgson, M. Avrigeanu, *Phys. Rev. C* 49 (1994) 2136.

- [9] G. La Rana et al., Phys. Rev. C 35 (1987) 373; G. D.J. Moses et al., Phys. Rev. C 36 (1987) 422; R. Lacey et al., Phys. Lett. B 191 (1987) 253; G. Bozzolo, O. Civitarese, J.P. Vary, Phys. Lett. B 219 (1989) 161.
- [10] M. Avrigeanu, W. von Oertzen, V. Avrigeanu, Nucl. Phys. A 764 (2006) 246.
- [11] P. Demetriou, C. Grama, S. Goriely, Nucl. Phys. A 707 (2002) 253.
- [12] M. Avrigeanu, W. von Oertzen, A.J.M. Plompen, V. Avrigeanu, Nucl. Phys. A 723 (2003) 104.
- [13] M. Avrigeanu, W. von Oertzen, A. Obreja, F.L. Roman, V. Avrigeanu, in Proc. of Int. Conf. on Nuclear Data for Science and Technology, Nice, France (2007) (in press).
- [14] Gy. Gyrky, G.G. Kiss, Z. Elekes, Zs. FLP, E. Samorjai, A. Palumbo, J. Görres, H.Y. Lee, W. Rapp, M. Wiescher, N. Özkan, R.T. Güray, G. Efe, T. Rauscher, Phys. Rev. C 74 (2006) 025805.
- [15] N. Özkan, G. Efe, R.T. Güray, A. Palumbo, J. Görres, H.Y. Lee, L.O. Lamm, W. Rapp, E. Stech, M. Wiescher, Gy. Gyrky, Zs. FLP, E. Samorjai, Phys. Rev. C 75 (2007) 025801.
- [16] L. McFadden, G.R. Satchler, Nucl. Phys. A84 (1966) 177.
- [17] T. Rauscher, Nucl. Phys. A 719 (2002) 73c; A725 (2003) 295(E).
- [18] P.E. Koehler, Yu.M. Gledenov, T. Rauscher, C. Fröhlich, Phys. Rev. C 69 (2004) 015803.
- [19] D. Galaviz, Zs. Fülöp, Gy. Gyürky, Z. Máté, P. Mohr, T. Rauscher, E. Somorjai, A. Zilges, Phys. Rev. C 71 (2005) 065802.
- [20] M.S. Basunia, E.B. Norman, H.A. Shugart, A.R. Smith, M.J. Dolinski, B.J. Quiter, Phys. Rev. C 71 (2005) 035801.
- [21] W. Rapp, M. Heil, D. Hentschel, R. Reifarth, H.J. Brede, H. Klein, T. Rauscher, Phys. Rev. C 66 (2002) 015803.
- [22] S. Harissopulos, A. Lagoyannis, A. Spyrou, Ch., Zarkadas, S. Galanopoulos, G. Perdikakis, H.-W. Becker, C. Rolfs, F. Strieder, R. Kunz, M. Fey, J.W. Hammer, A. Dewald, K.-O. Zell, P. von Brentano, R. Julin, P. Demetriou, J. Phys. G: Nucl. Part. Phys. 31 (2005) S1417.
- [23] A. Kumar, S. Kailas, S. Rathi, K. Mahata, Nucl. Phys. A 776 (2006) 105.
- [24] U. Atzrott, P. Mohr, H. Abele, C. Hillenmayer, G. Staudt, Phys. Rev. C 53 (1996) 1336.
- [25] Zs. Fülöp, Gy. Gyürky, Z. Máté, E. Somorjai, L. Zolnai, D. Galaviz, M. Babilon, P. Mohr, A. Zilges, T. Rauscher, H. Oberhammer, G. Staudt, Phys. Rev. C 64 (2001) 065805.

- [26] G.G. Kiss, Zs. Flp, Gy. Gyrky, Z. Mt, E. Samorjai, D. Galaviz, S. Müller, A. Zilges, P. Mohr, M. Avrigeanu, J. Phys. G: Nucl. Part. Phys. 35 (2008), doi:10.1088/0954-3899/35/1/014037.
- [27] M. Avrigeanu, V. Avrigeanu, Phys. Rev. C 73 (2006) 038801.
- [28] H. Vonach, R.C. Haight, G. Winkler, Phys. Rev. C 28 (1983) 2278.
- [29] P. Reimer, V. Avrigeanu, A.J.M. Plompen, S.M. Qaim, Phys. Rev. C 65 (2001) 014604.
- [30] V. Semkova, V. Avrigeanu, T. Glodariu, A.J. Koning, A.J.M. Plompen, D.L. Smith, S. Sudar, Nucl. Phys. A 730 (2004) 255.
- [31] M. Avrigeanu, S.V. Chuvaev, A.A. Filatenkov, R.A. Forrest, M. Herman, A.J. Koning, A.J.M. Plompen, F.L. Roman, V. Avrigeanu, arXiv:0712.0699 [nucl-ex]; Nucl. Phys. A 608 (2008) 15.
- [32] P. Reimer, V. Avrigeanu, S. Chuvaev, A.A. Filatenkov, T. Glodariu, A.J. Koning, A.J.M. Plompen, S.M. Qaim, D.L. Smith, H. Weigmann, Phys. Rev. C 71 (2005) 044617.
- [33] V. Avrigeanu, F.L. Roman, M. Avrigeanu, in: A. Plompen (Ed.), Proc. 4th NEMEA-4 Workshop on Neutron Measurements, Evaluations and Applications, Prague, Czechia (2007), European Commission Report EUR 23235 EN, Belgium, 2008, p. 143. Available from: www.irmm.jrc.be/html/publications/.
- [34] M. Avrigeanu, V. Avrigeanu, A. Obreja, F.L. Roman, OECD/NEA Data Bank Report EFFDOC-1022, Nov. 2007.
- [35] G.R. Satchler, W.G. Love, Phys. Rep. 55 (1979) 183.
- [36] M.E. Brandan, G.R. Satchler, Phys. Rep. 285 (1997) 143.
- [37] Dao T. Khoa, Phys. Rev. C 63 (2001) 034007.
- [38] G. Bertsch, J. Borysowicz, H. McManus, W.G. Love, Nucl. Phys. A 284 (1977) 399.
- [39] N. Anantaraman, H. Toki, G. Bertsch, Nucl. Phys. A 398 (1983) 279.
- [40] Dao T. Khoa, G.R. Satchler, Nucl. Phys. A668 (2000) 3.
- [41] Dao T. Khoa, W. von Oertzen, Phys. Lett. B 304 (1993) 8; 342 (1995) 6; Dao T. Khoa, W. von Oertzen, H.G. Bohlen, Phys. Rev. C 49 (1994) 1652; Dao T. Khoa, W. von Oertzen, A.A. Ogloblin, Nucl. Phys. A 602 (1996) 98.
- [42] D.T. Khoa, G.R. Satchler, W. von Oertzen, Phys. Rev. C 56 (1997) 954.
- [43] D. Baye, L. Desorgher, D. Guillaïn, D. Herschkowitz, Phys. Rev. C 54 (1996) 2563.
- [44] I. Tanihata, D. Hirata, T. Kobayashi, S. Shimoura, K. Sugimoto, H. Toki, Preprint RIKEN-AF-NP-123, 1992; Phys. Lett. B 289 (1992) 261.

- [45] J.W. Negele, Phys. Rev. C 1 (1970) 1260.
- [46] J.W. Lightbody, Jr., S. Penner, S.P. Fivozinsky, P.L. Hallowell, H. Crannell, Phys. Rev. C 14 (1976) 952.
- [47] M. El-Azab Farid, G.R. Satchler, Nucl. Phys. A 438 (1985) 525.
- [48] A.M. Kobos, B.A. Brown, P.E. Hodgson, G.R. Satchler, A. Budzanowski, Nucl. Phys. A 384 (1982) 65.
- [49] H. Abele, G. Staudt, Phys. Rev. C 47 (1993) 742.
- [50] A. Ingemarsson, J. Nyberg, P.U. Renberg, O. Sundberg, R.F. Carlson, A.J. Cox, A. Auce, R. Johansson, G. Tibell, Dao T. Khoa, R.E. Warner, Nucl. Phys. A 676 (2000) 3.
- [51] C. Mahaux, H. Ngo, G.R. Satchler, Nucl. Phys. A 449 (1986) 354.
- [52] C. Mahaux, H. Ngo, G.R. Satchler, Nucl. Phys. A 456 (1986) 134.
- [53] G.R. Satchler, Phys. Rep. 199 (1991) 147.
- [54] H.P. Gubler, U. Kiebele, H.O. Meyer, G.R. Plattner, I. Sick, Nucl. Phys. A 351 (1981) 29; EXFOR-D0257 data file entry, EXFOR Nuclear Reaction Data, <http://www-nds.iaea.or.at/exfor> .
- [55] F. Ballester, E. Casal, J.B.A. England, Nucl. Phys. A 513 (1990) 61; EXFOR-01087 data file entry.
- [56] A. Bredbacka, M. Brenner, K.M. Kallman, P. Manngard, Z. Mate, S. Szilagyi, L. Zolnai, Nucl. Phys. A 574 (1994) 397; EXFOR-F0461 data file entry.
- [57] F. Ballester, E. Casal, J.B.A. England, Nucl. Phys. A 501 (1989) 301; EXFOR-F0528 data file entry.
- [58] A.G. Blair, H.E. Wegner, Phys. Rev. 127 (1962) 1233; EXFOR-C1022 data file entry.
- [59] F. Ballester, E. Casal, J. Diaz, J.B.A. England, F. Moriano, J. Phys. G 13 (1987) 1541; EXFOR-01089 data file entry.
- [60] L.R. Gasques et al., Phys. Rev. C 67 (2003) 024602; EXFOR-C1165 data file entry.
- [61] W. Trombik, K.A. Eberhard, O. Hinderer, H.H. Rossner, A. Weidinger, J.S. Eck, Phys. Rev. C 9 (1974) 1813; EXFOR-D0372 data file entry.
- [62] A. Budzanowski et al., Phys. Rev. C 17 (1978) 951; EXFOR-D0296 data file entry.
- [63] U. Kiebele, E. Baumgartner, H.P. Gubler, H.O. Meyer, G.R. Plattner, I. Sick, Helvetica Physica Acta 51 (1978) 726; EXFOR-D0373 data file entry.
- [64] A.A. Cowley, P.M. Cronje, G. Heymann, S.J. Mills, J.C. van Staden, Nucl. Phys. A 229 (1974) 256; EXFOR-D0374 data file entry.

- [65] F. Ballester, E. Casal, J.B.A. England, F. Moriano, Nucl. Phys. A 490 (1988) 227; EXFOR-F0077 data file entry.
- [66] F. Ballester, E. Casal, J.B.A. England, F. Moriano, J. Phys. G 14 (1988) 1103; EXFOR-O1088 data file entry.
- [67] M. Wit, J. Schiele, K.A. Eberhard, J.P. Schiffer, Phys. Rev. C 12 (1975) 1447; EXFOR-D0345 data file entry.
- [68] B.D. Watson, D. Robson, D.D. Tolbert, R.H. Davis, Phys. Rev. C 4 (1971) 2240.
- [69] O.V. Bespalova, E.A. Romanovskij, N.G. Gorjaga, Nguen Mak Kha, B.S. Galakhmatova, Luaj Morzena Rafu, S.I. Fedoseev, Dang Lam, Anis Belal, Yad. Fiz. 56 (1992) 113; EXFOR-A0545 data file entry.
- [70] O. Bersillon, Centre d'Etudes de Bruyeres-le-Chatel, Note CEA-N-2227, 1992.
- [71] P. Mohr, T. Rauscher, H. Oberhummer, Z. Máté, Zs. Fülöp, E. Somorjai, M. Jaeger, G. Staudt, Phys. Rev. C 55 (1997) 1523.
- [72] R.M. Drisko, G.R. Satchler, R.H. Bassel, Phys. Lett. 5 (1963) 347.
- [73] W. Nörenberg, in: Heavy Ion Collisions, R. Bock (Ed.), North-Holland, Amsterdam, 1980.
- [74] P. Mohr, Phys. Rev. C 61 (2000) 045802.
- [75] M. Avrigeanu, V. Avrigeanu, Report NP-86-1995, Bucharest, IPNE, 1995; News NEA Data Bank 17 (1995) 22.
- [76] G.E. Brown, M. Rho, Nucl. Phys. A 372 (1981) 397.
- [77] E. Somorjai, Zs. Fülöp, A.Z. Kiss, C.E. Rolfs, H.-P. Trautvetter, U. Greife, M. Junker, S. Goriely, M. Arnould, M. Rayet, T. Rauscher, H. Oberhummer, Astron. Astrophys. 333 (1998) 1112.
- [78] A.J. Morton, S.G. Tims, A.F. Scott, V.Y. Hansper, C.I.W. Tingwell, D.G. Sargood, Nucl. Phys. A 537 (1992) 167.
- [79] C.M. Baglin, E.R. Norman, R.M. Larimer, G.A. Rech, AIP Conf. Proc. 769 (2005) 1370.
- [80] A.E. Vlieks, J.F. Morgan, S.L. Blatt, Nucl. Phys. A 224 (1974) 492.
- [81] V.Y. Hansper, A.J. Morton, S.G. Tims, C.I.W. Tingwell, A.F. Scott, D.G. Sargood, Nucl. Phys. A 551 (1993) 158.
- [82] Xiufeng Peng, Fuqing He, Xianguan Long, Nucl. Inst. Meth. B 152 (1999) 432.
- [83] V.Y. Hansper, C.I.W. Tingwell, S.G. Tims, A.F. Scott, D.G. Sargood, Nucl. Phys. A 504 (1989) 605.
- [84] A.J. Howard, H.B. Jensen, M. Rios, W.A. Fowler, B.A. Zimmerman, Astrophys. J. 188 (1974) 131; EXFOR-C0180 data file entry.

- [85] A.J. Morton, A.F. Scott, S.G. Tims, V.Y. Hansper, D.G. Sargood, Nucl. Phys. A 573 (1994) 276.
- [86] S.G. Tims, A.J. Morton, C.I.W. Tingwell, A.F. Scott, V.Y. Hansper, D.G. Sargood, Nucl. Phys. A 524 (1991) 479.
- [87] A.A. Sonzogni et al., Phys. Rev. Lett. 84 (2000) 1651.
- [88] S.G. Tims, A.F. Scott, A.J. Morton, V.Y. Hansper, D.G. Sargood, Nucl. Phys. A 563 (1993) 473.
- [89] F.K. McGowan, P.H. Stelson, W.G. Smith, Phys. Rev. 133 (1964) B907.
- [90] M. Rios, B.D. Anderson, J.S. Schweitzer, Nucl. Phys. A 236 (1974) 523.
- [91] J.L. Zyskind, J.M. Davidson, M.T. Esat, M.H. Shapiro, R.H. Spear, Nucl. Phys. A 331 (1979) 180.
- [92] M.E. Sevier, L.M. Mitchell, C.I.W. Tingwell, D.G. Sargood, Nucl. Phys. A 454 (1986) 128.
- [93] M.R. Anderson, S.R. Kennett, Z.E. Switkowski, D.G. Sargood, Nucl. Phys. A 318 (1979) 471.
- [94] P.H. Stelson, F.K. McGowan, Phys. Rev. 133 (1964) B911.
- [95] J.M. D'Auria, M.J. Fluss, L. Kowalski, J.M. Miller, Phys. Rev. 168 (1968) 1224.
- [96] O.A. Zhukova, V.I. Kanashevich, S.V. Laptev, G.P. Chursin, Sov. J. Nucl. Phys. 16 (1973) 134; EXFOR-A0644 data file entry.
- [97] F.M. Mann, R.W. Kavanach, Nucl. Phys. A 255 (1975) 287.
- [98] S.G. Tims, C.I.W. Tingwell, V.Y. Hansper, A.F. Scott, D.G. Sargood, Nucl. Phys. A 483 (1988) 354.
- [99] N.T. Porile, D.L. Morrison, Phys. Rev. 116 (1959) 1193.
- [100] J. Zweit, H. Sharma, S. Downey, Appl. Radiat. Isot. 38 (1987) 499; EXFOR-D0119 data file entry.
- [101] N.L. Singh, B.J. Patel, D.R.S. Somayajulu, S.N. Chintalapudi, Pramana 42 (1994) 349; EXFOR-D0099 data file entry.
- [102] Zs. Fulop, A.Z. Kiss, E. Somorjai, C.E. Rolfs, H.P. Trautvetter, T. Rauscher, H. Oberhummer, Z. Phys. A 355 (1996) 203; EXFOR-O0897 data file entry.

Table 1

The experimental data of α -particle elastic scattering analysed in this work.

Target	E_α (MeV)	Ref.
^{50}Ti	24.97, 27.06, 29.06, 31, 33, 35.06, 37.12, 39, 41.05, 43, 44.98, 46.8	[54]
^{51}V , $^{50,52,53}\text{Cr}$, ^{59}Co , ^{63}Cu	25	[55]
^{50}Cr , ^{62}Ni	12.8, 14.56, 16.34, 18.13	[56]
^{52}Cr	23, 24.97, 27.06, 29.1, 31, 33, 35.06, 37.12, 39, 41.05, 43, 44.98, 46.8	[54]
$^{56,58}\text{Fe}$	25	[57]
^{56}Fe	26.45	[58]
$^{58,60,62,64}\text{Ni}$	25	[59]
^{58}Ni	8.1, 9.1, 9.6	[60]
$^{58,60,62,64}\text{Ni}$	18, 21, 24.1, 27	[61]
^{58}Ni	26.5, 29, 34, 38	[62]
^{60}Ni	29, 34	[62]
^{58}Ni	37, 43, 49	[63]
$^{58,60,62,64}\text{Ni}$	32.3	[64]
$^{70,72,74,76}\text{Ge}$	25	[65]
$^{76,78,80}\text{Se}$	25	[66]
^{89}Y , $^{90,91}\text{Zr}$	21, 23.4, 25	[67]
^{90}Zr , ^{107}Ag	15	[68]
^{92}Mo	13.83, 16.42, 19.5	[25]
^{94}Mo , ^{107}Ag , $^{116,122,124}\text{Sn}$	25.2	[69]
^{89}Y	16.2, 19.44	[26]
^{112}Sn	14.4	[19]
$^{112,124}\text{Sn}$	19.5	[19]

Table 2: Optical potential parameters and volume integrals (without the negative sign) obtained by fits of the α -particle elastic-scattering data for A=50–124 nuclei at energies ≤ 50 MeV. E_α , V_R , W_V and W_D are in MeV, r_R and a_R are in fm, J_R , J_V and J_D are in MeV·fm³.

Target	E_α (MeV)	V_R (MeV)	r_R (fm)	a_R (fm)	W_V (MeV)	W_D (MeV)	J_R (MeV·fm ³)	J_V (MeV·fm ³)	J_D (MeV·fm ³)
⁵⁰ Ti	24.97	111	1.498	0.540	19.8	2.93	427	55.0	10.8
	27.06	53.0	1.612	0.522	22.2	0	250	61.4	0
	29.06	138	1.452	0.552	24.4	0	489	67.6	0
	31.0	101	1.482	0.572	26.5	0	381	73.6	0
	33.0	106.5	1.468	0.572	28.8	0	392	79.7	0
	35.06	109.5	1.474	0.558	31.0	0	405	86.1	0
	37.12	89.5	1.514	0.550	33.3	0	356	92.4	0
	39.0	91.5	1.510	0.546	35.4	0	361	98.2	0
	41.05	92.0	1.518	0.540	37.7	0	368	105.0	0
	43.0	99.5	1.502	0.532	39.9	0	385	111	0
	44.98	106	1.500	0.524	42.0	0	408	117	0
	46.8	112	1.492	0.516	44.1	0	423	122	0
⁵¹ V	25.0	115	1.476	0.562	19.8	3.0	427	54.8	10.9
⁵⁰ Cr	12.8	188	1.236	0.700	6.3	20.5	458	17.6	75.4
	14.56	105	1.536	0.568	8.3	18.0	438	23.0	66.0
	16.34	136	1.328	0.660	10.3	15.4	393	28.4	56.6
	18.13	103	1.466	0.612	12.2	12.8	383	34.0	47.1
	25.0	109	1.506	0.562	19.9	2.9	429	55.1	10.6
⁵² Cr	23.0	103.5	1.516	0.538	17.5	6.0	411	48.4	21.6
	24.97	106	1.514	0.524	19.7	3.1	418	54.6	11.2
	27.06	113.5	1.510	0.512	22.0	0.1	442	60.9	0.45
	29.1	119.5	1.504	0.506	24.3	0	460	67.2	0
	31.0	98.5	1.502	0.546	26.4	0	382	73.0	0
	33.0	109	1.446	0.592	28.6	0	386	79.2	0

Table 2: continued.

Target	E_α (MeV)	V_R (MeV)	r_R (fm)	a_R (fm)	W_V (MeV)	W_D (MeV)	J_R (MeV·fm ³)	J_V (MeV·fm ³)	J_D (MeV·fm ³)
	35.06	109	1.492	0.536	30.9	0	414	85.5	0
	37.12	131.5	1.412	0.596	33.2	0	436	91.8	0
	39.0	128.5	1.436	0.570	35.3	0	443	97.6	0
	41.05	91.5	1.496	0.566	37.5	0	353	104	0
	43.0	95.5	1.488	0.562	39.7	0	362	110	0
	44.98	96	1.476	0.566	41.9	0	357	116	0
	46.8	109	1.468	0.558	43.9	0	398	122	0
⁵³ Cr	25.0	111.5	1.492	0.552	19.7	3.2	425	54.3	11.4
⁵⁶ Fe	25.0	102	1.512	0.554	19.5	3.5	402	53.6	12.2
	26.45	108.5	1.478	0.554	21.1	1.4	401	58.0	4.94
⁵⁸ Fe	25.0	134.5	1.390	0.616	19.3	3.7	427	53.1	12.6
⁵⁹ Co	25.0	121	1.438	0.584	19.3	3.8	417	52.9	12.8
⁵⁸ Ni	8.1	70	1.858	0.354	0.6	25.9	481	1.57	87.5
	9.1	79.5	1.718	0.436	1.7	25.9	502	4.63	87.5
	9.6	78.5	1.664	0.466	2.2	22.5	398	6.15	76.0
	18.0	59.5	1.862	0.490	11.6	13.9	420	31.8	46.8
	21.0	77	1.670	0.570	14.9	9.5	404	40.9	32.2
	24.1	104	1.476	0.574	18.3	5.0	385	50.4	17.0
	25.0	103.5	1.504	0.558	19.3	3.7	402	53.1	12.6
	26.5	112.5	1.466	0.558	21.0	1.6	406	57.7	5.29
	27.0	169.5	1.236	0.662	21.6	0.8	398	59.2	2.85
	29.0	120.5	1.458	0.556	23.8	0	428	65.4	0
	32.3	134.5	1.412	0.570	27.4	0	439	75.4	0
	34.0	209	1.426	0.516	29.3	0	688	80.6	0
	37.0	140	1.384	0.597	32.7	0	436	89.8	0
	38.0	139	1.400	0.572	33.8	0	443	92.8	0

Table 2: continued.

Target	E_α	V_R	r_R	a_R	W_V	W_D	J_R	J_V	J_D
	(MeV)	(MeV)	(fm)	(fm)	(MeV)	(MeV)	(MeV·fm ³)	(MeV·fm ³)	(MeV·fm ³)
⁶⁰ Ni	43.0	99.5	1.502	0.524	39.3	0	381	108	0
	49.0	73.5	1.600	0.482	46.0	0	334	126	0
	18.0	143.5	1.522	0.526	11.4	14.1	570	31.4	46.6
	21.0	136.5	1.416	0.604	14.8	9.7	453	40.5	32.2
	24.1	129.5	1.388	0.636	18.2	5.2	411	50.0	17.4
	25.0	99.5	1.520	0.566	19.2	3.9	398	52.7	13.1
	27.0	139	1.364	0.592	21.4	1.0	414	58.8	3.46
	29.0	106	1.520	0.506	23.6	0	417	64.9	0
	32.3	127	1.434	0.560	27.3	0	430	74.9	0
⁶² Ni	34.0	149	1.458	0.540	29.2	0	526	80.1	0
	12.8	162	1.286	0.684	5.5	21.8	425	15.2	70.8
	14.56	162.5	1.428	0.574	7.5	19.2	546	20.5	62.5
	16.34	132	1.440	0.586	9.5	16.6	456	25.9	54.2
	18.0	151	1.310	0.652	11.3	14.3	411	31.0	46.4
	18.13	139.5	1.378	0.622	11.5	14.1	431	31.4	45.8
	21.0	127	1.454	0.574	14.6	9.9	449	40.1	32.3
	24.1	100.5	1.508	0.582	18.1	5.4	395	49.5	17.7
	25.0	125.5	1.412	0.622	19.1	4.1	415	52.3	13.4
⁶⁴ Ni	27.0	106.5	1.500	0.534	21.3	1.2	406	58.3	4.04
	32.3	119.5	1.444	0.560	27.2	0	412	74.5	0
	18.0	167.5	1.224	0.744	11.2	14.4	395	30.6	46.1
	21.0	112	1.524	0.566	14.5	10.1	450	39.7	32.3
	24.1	115	1.462	0.604	18.0	5.6	416	49.1	18.0
	25.0	115	1.454	0.596	19.0	4.3	408	51.8	13.8
	27.0	96.5	1.550	0.534	21.2	1.4	404	57.9	4.58
	32.3	115.5	1.466	0.548	27.1	0	414	74.0	0

Table 2: continued.

Target	E_α (MeV)	V_R (MeV)	r_R (fm)	a_R (fm)	W_V (MeV)	W_D (MeV)	J_R (MeV·fm ³)	J_V (MeV·fm ³)	J_D (MeV·fm ³)
⁶³ Cu	25.0	114.5	1.464	0.580	19.0	4.2	413	52.1	13.6
⁷⁰ Ge	25.0	103.5	1.500	0.566	18.6	4.9	396	50.7	14.8
⁷² Ge	25.0	90.5	1.556	0.548	18.5	5.1	382	50.3	15.1
⁷⁴ Ge	25.0	115.5	1.420	0.614	18.4	5.2	382	49.9	15.3
⁷⁶ Ge	25.0	115	1.428	0.614	18.3	5.4	386	49.6	15.6
⁷⁶ Se	25.0	113	1.520	0.592	18.3	5.4	450	49.6	15.6
⁷⁸ Se	25.0	109.5	1.440	0.602	18.2	5.6	375	49.2	15.8
⁸⁰ Se	25.0	111.5	1.520	0.578	18.1	5.7	441	48.9	16.1
⁸⁹ Y	16.2	133	1.404	0.606	7.9	19.2	421	21.1	50.2
	19.44	136	1.356	0.634	11.4	14.5	393	30.8	38.0
	21.0	122	1.438	0.552	13.2	12.2	407	35.5	32.1
	23.4	110.5	1.468	0.574	15.8	8.8	394	42.7	23.0
	25.0	115	1.472	0.540	17.6	6.4	409	47.4	16.9
⁹⁰ Zr	15.0	167.5	1.310	0.656	6.5	21.0	443	17.4	54.6
	21.0	125	1.426	0.566	13.1	12.3	409	35.3	32.0
	23.4	107.5	1.486	0.550	15.8	8.8	394	42.5	23.0
	25.0	115	1.464	0.550	17.6	6.5	404	47.3	17.0
⁹¹ Zr	21.0	122	1.440	0.558	13.1	12.4	409	35.2	32.0
	23.0	105.5	1.500	0.542	15.3	9.5	396	41.2	24.5
	25.0	114.5	1.474	0.536	17.5	6.6	409	47.1	17.1
⁹² Mo	13.83	188.5	1.228	0.704	5.1	22.8	423	13.7	58.6
	16.42	149.5	1.372	0.602	8.0	19.1	442	21.4	49.0
	19.5	164.5	1.346	0.610	11.4	14.6	462	30.6	37.5
⁹⁴ Mo	25.2	136.5	1.438	0.534	17.6	6.5	453	47.3	16.5
¹⁰⁷ Ag	15.0	117.5	1.484	0.534	5.7	22.2	425	15.3	51.7
	25.2	167.5	1.252	0.700	17.0	7.5	391	45.5	17.4

Table 2: continued.

Target	E_α (MeV)	V_R (MeV)	r_R (fm)	a_R (fm)	W_V (MeV)	W_D (MeV)	J_R (MeV·fm ³)	J_V (MeV·fm ³)	J_D (MeV·fm ³)
¹¹² Sn	14.4	101.5	1.566	0.476	4.8	23.4	424	12.9	52.9
	19.5	138.5	1.420	0.574	10.5	16.0	444	28.0	36.2
¹¹⁶ Sn	25.2	130.5	1.442	0.550	16.7	8.0	434	44.4	17.8
¹²² Sn	25.2	113.5	1.492	0.524	16.4	8.4	414	43.7	18.0
¹²⁴ Sn	19.5	130	1.424	0.578	10.0	16.8	419	26.6	35.4
	25.2	101.5	1.580	0.508	16.3	8.5	436	43.4	18.0

Table 3

Optical potential parameters of the regional potential (ROP). The energies are in MeV and geometry parameters in fm.

Potential depth (MeV)		Geometry parameters (fm)	
$V_R=168+0.733Z/A^{1/3}-2.64E,$	$E < E_3$	$r_R=1.18+0.012E,$	$E < 25$
$=116.5+0.337Z/A^{1/3}-0.453E,$	$E \geq E_3$	$=1.48,$	$E \geq 25$
		$a_R=0.671+0.0012A+(0.0094-0.0042A^{1/3})E_2,$	$E < E_2$
		$=\max$	$E \geq E_2$
		$(0.671+0.0012A+(0.0094-0.0042A^{1/3})E,$	
		$0.55),$	
$W_V=2.73-2.88A^{1/3}+1.11E$		$r_V=1.34$	
		$a_V=0.50$	
$W_D=4,$	$E < E_1$	$r_D=1.52$	
$=22.2+4.57A^{1/3}-7.446E_2+6E,$	$E_1 < E < E_2$	$a_D=0.729-0.074A^{1/3}$	
$=22.2+4.57A^{1/3}-1.446E,$	$E_2 < E$		

where:

$$E_1=-3.03-0.762A^{1/3}+1.24E_2 \quad E_2=(2.59+10.4/A)Z/R_B \quad E_3=23.6+0.181Z/A^{1/3}$$

$$R_B=2.66+1.36A^{1/3} \quad [73]$$

Figure captions

Fig. 1. (Color online) Comparison of experimental (see Table 1) angular distributions of the elastic scattering of α -particles at 25 MeV on ^{51}V , ^{53}Cr , $^{56,58}\text{Fe}$, ^{59}Co , ^{63}Cu , $^{70,74,76}\text{Ge}$, $^{76,78,80}\text{Se}$, ^{94}Mo , ^{107}Ag and $^{112,124}\text{Sn}$, divided by the Rutherford cross section, with OMP calculations by using either the present local parameter sets of Table 2 (solid curves), the regional parameter set in Table 3 (dash-dotted curves), or the global OMP parameter set of Kumar et al. [23] (dotted curves).

Fig. 2. (Color online) The same as in Fig. 1 but for α -particles scattered on ^{50}Ti between 25 and 47 MeV.

Fig. 3. (Color online) The same as in Fig. 1 but for α -particles scattered on ^{52}Cr between 23 and 47 MeV.

Fig. 4. (Color online) The same as in Fig. 1 but for α -particles scattered on ^{50}Cr between 13 and 25 MeV, and ^{62}Ni between 13 and 32 MeV.

Fig. 5. (Color online) The same as in Fig. 1 but for α -particles scattered on ^{60}Ni between 18 and 34 MeV, and ^{64}Ni between 18 and 32 MeV.

Fig. 6. (Color online) The same as in Fig. 1 but for α -particles scattered on ^{58}Ni between 8 and 49 MeV.

Fig. 7. (Color online) The same as in Fig. 1 but for α -particles scattered on ^{89}Y , $^{90,91}\text{Zr}$, ^{94}Mo , ^{107}Ag and $^{112,124}\text{Sn}$, between 14 and 25 MeV.

Fig. 8. The χ^2 deviation per degree of freedom between the experimental and calculated angular distributions of the elastic scattering of α -particles on ^{112}Sn at 14.4 MeV, versus the real potential depth V_R (solid curve), as well as the values of the real-potential radius r_R , diffuseness a_R and volume integral per interacting nucleon pair J_R , corresponding to the χ^2 minima. The dotted curves are drawn to guide the eye.

Fig. 9. The real-potential diffuseness a_R obtained by analysis of the experimental angular distributions of α -particle elastic scattering (Table 1) using the average values for the rest of all OMP parameters (Table 3), versus the α -particle energy (top) and its ratio in the center-of-mass system to the Coulomb barrier B_C (bottom). The full circles correspond to the target nuclei with $A > 89$.

Fig. 10. (Color online) Comparison of measured [60] angular distributions of the elastic scattering of α -particles between 8.1 and 9.6 MeV on ^{58}Ni , with OMP calculations using (a) the local imaginary-potential parameters (Table 2) and semi-microscopic DF approach together with the surface-imaginary po-

tential dispersive corrections formerly used within the elastic–scattering analysis (dotted curves) and corresponding to the final form of the ROP surface imaginary–potential in Table 3 (solid curves), and (b) the phenomenological parameters obtained formerly within the elastic–scattering analysis, i.e. for energies above the limit E_2 in Table 3 (dashed curves), and the final ROP (solid curves). In the inset of (a) are shown the same surface–imaginary potential dispersive corrections used for calculation of the angular distributions shown by the similar curves.

Fig. 11. (Color online) Comparison of measured total α -reaction cross sections for ^{48}Ti and ^{51}V [28], and the related (α, n) reaction cross sections for ^{48}Ti [28,78,79] and ^{51}V [28,80,81,82], as well as for ^{45}Sc [80,83], ^{46}Ti [80,84], ^{50}Cr [80,85] and ^{54}Fe [80,86], and $^{44}\text{Ti}(\alpha, p)^{47}\text{V}$ reaction cross sections [87], with calculated values using the predictions of the present optical potential established by the elastic–scattering data analysis alone at energies above the Coulomb barrier B_C (dash–dotted curves) as well as its final form (Table 3) proved necessary for the (α, x) reaction data account (solid curves).

Fig. 12. (Color online) Comparison of measured (α, γ) , (α, n) and (α, p) reaction cross sections for ^{55}Mn [88], ^{58}Ni [80,89,90], ^{62}Ni [91,92], and ^{64}Ni [91] target nuclei, and calculated values using the predictions of the present optical potential established by the elastic–scattering data analysis alone at energies above the Coulomb barrier B_C (dash–dotted curves), as well as a constant real–potential diffuseness a_R at lowest energies below the energy E_2 given in Table 3 (dashed curves), and the final ROP proved necessary for the (α, x) reaction data account (solid curves). The total α -reaction cross sections provided at all energies by the ROP parameters established by the elastic–scattering analysis alone, are also shown (dotted curves) for a direct view of the weight of reactions being analyzed, by comparison with the corresponding dash–dotted curves.

Fig. 13. (Color online) The same as in Fig. 12 but for the target nuclei ^{56}Fe [93], ^{59}Co [94,95,96,97,98], ^{63}Cu [20,94,97,99,100], ^{65}Cu [94,97,99,101], and ^{70}Ge [102].

Fig. 14. (Color online) The same as in Fig. 12 but for the target nuclei $^{96,98}\text{Ru}$ [21].

Fig. 15. (Color online) The same as in Fig. 12 but for the target nuclei ^{106}Cd [14] and $^{112,118}\text{Sn}$ [15,22], except the bottom–right corner where the final ROP proved necessary for the (α, x) reaction data account is used for all calculated cross sections of (α, n) (thick solid curve), (α, γ) (thin solid curve), (α, α') (short–dotted curve), and (α, p) (dash–dot–dotted curve) reactions.

Fig. 16. (Color online) The energies E_1 (dash–dotted curve) below which the imaginary–potential depth $W_D=4$ MeV, E_2 (solid curve) corresponding to

$0.9B_C$, and E_3 (dotted curve), at which the present ROP parameters change their energy dependences, versus the target nuclei atomic-mass number, and the energy ranges of the (α, x) reaction data formerly analyzed in the present work (thin vertical bars) as well as involved within the additional check of ROP (thick bars). The mass-dependences corresponding to nuclei with a nuclear asymmetry $(N-Z)/A$ value of 0.1 are shown, while the complete formulas of the energies E_1 , E_2 , E_3 are given in Table 3.

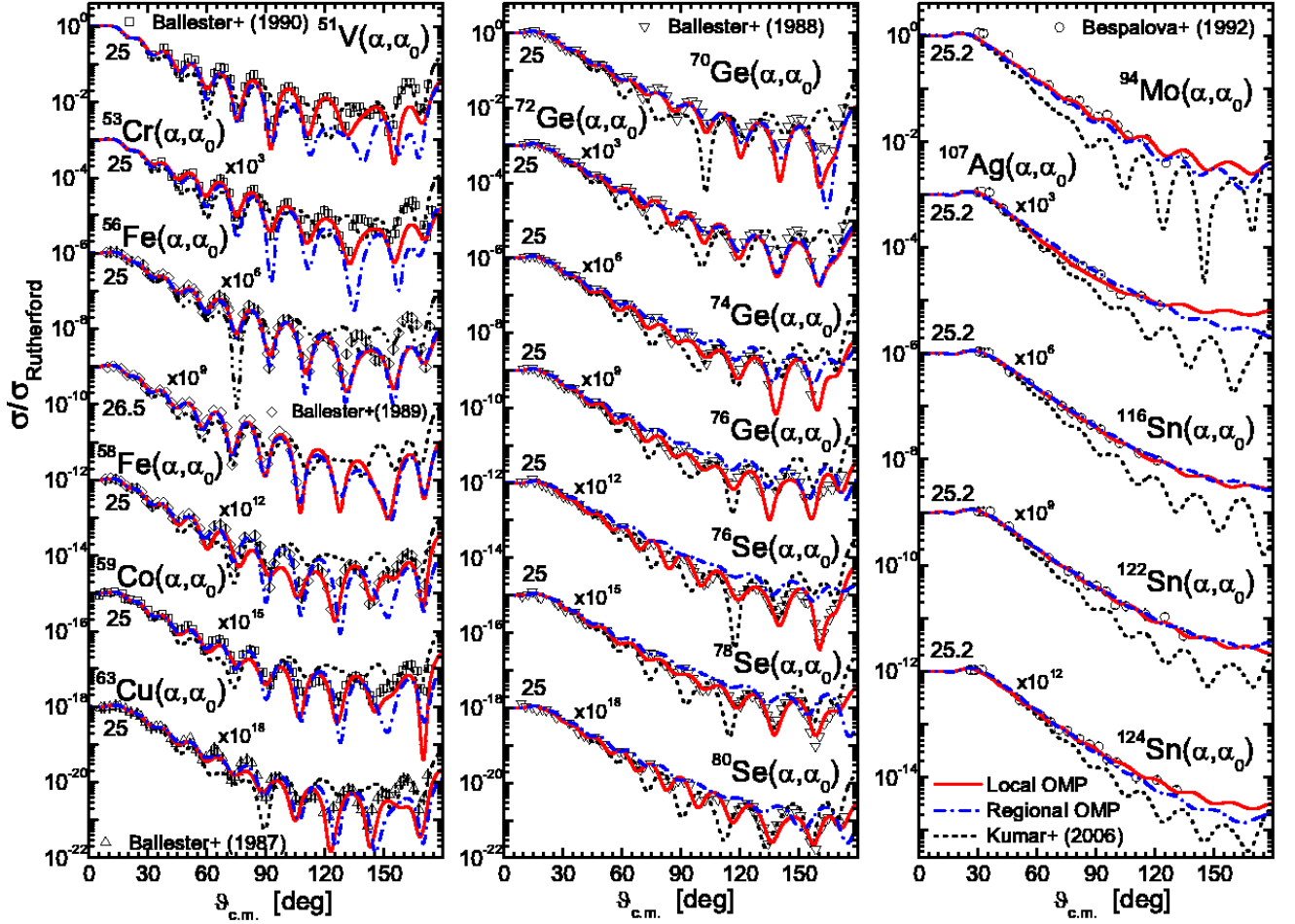


Fig. 1. (Color online) Comparison of experimental (see Table 1) angular distributions of the elastic scattering of α -particles at 25 MeV on ^{51}V , ^{53}Cr , $^{56,58}\text{Fe}$, ^{59}Co , ^{63}Cu , $^{70,74,76}\text{Ge}$, $^{76,78,80}\text{Se}$, ^{94}Mo , ^{107}Ag and $^{112,124}\text{Sn}$, divided by the Rutherford cross section, with OMP calculations by using either the present local parameter sets of Table 2 (solid curves), the regional parameter set in Table 3 (dash-dotted curves), or the global OMP parameter set of Kumar et al. [23] (dotted curves).

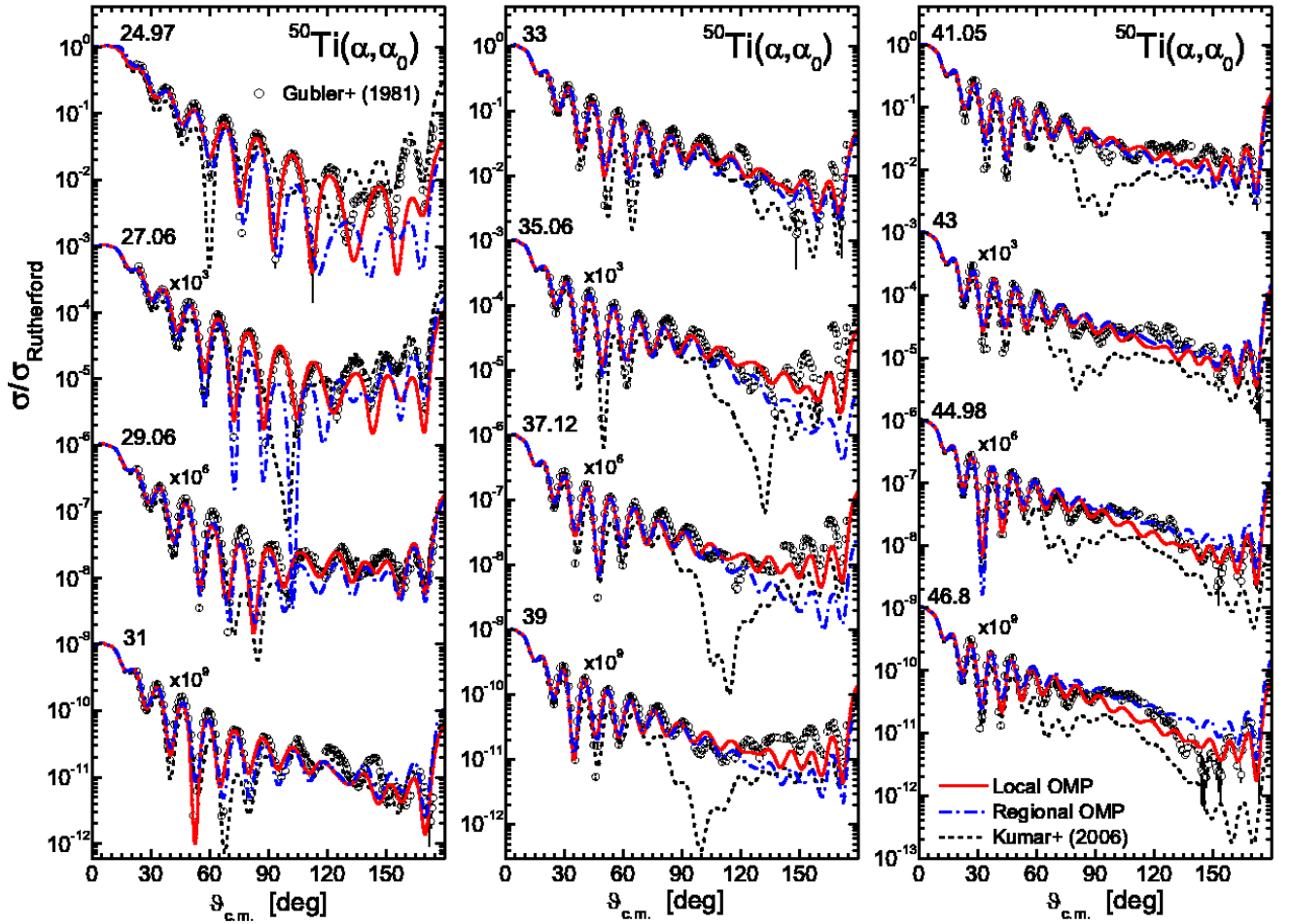


Fig. 2. (Color online) The same as in Fig. 1 but for α -particles scattered on ^{50}Ti between 25 and 47 MeV.

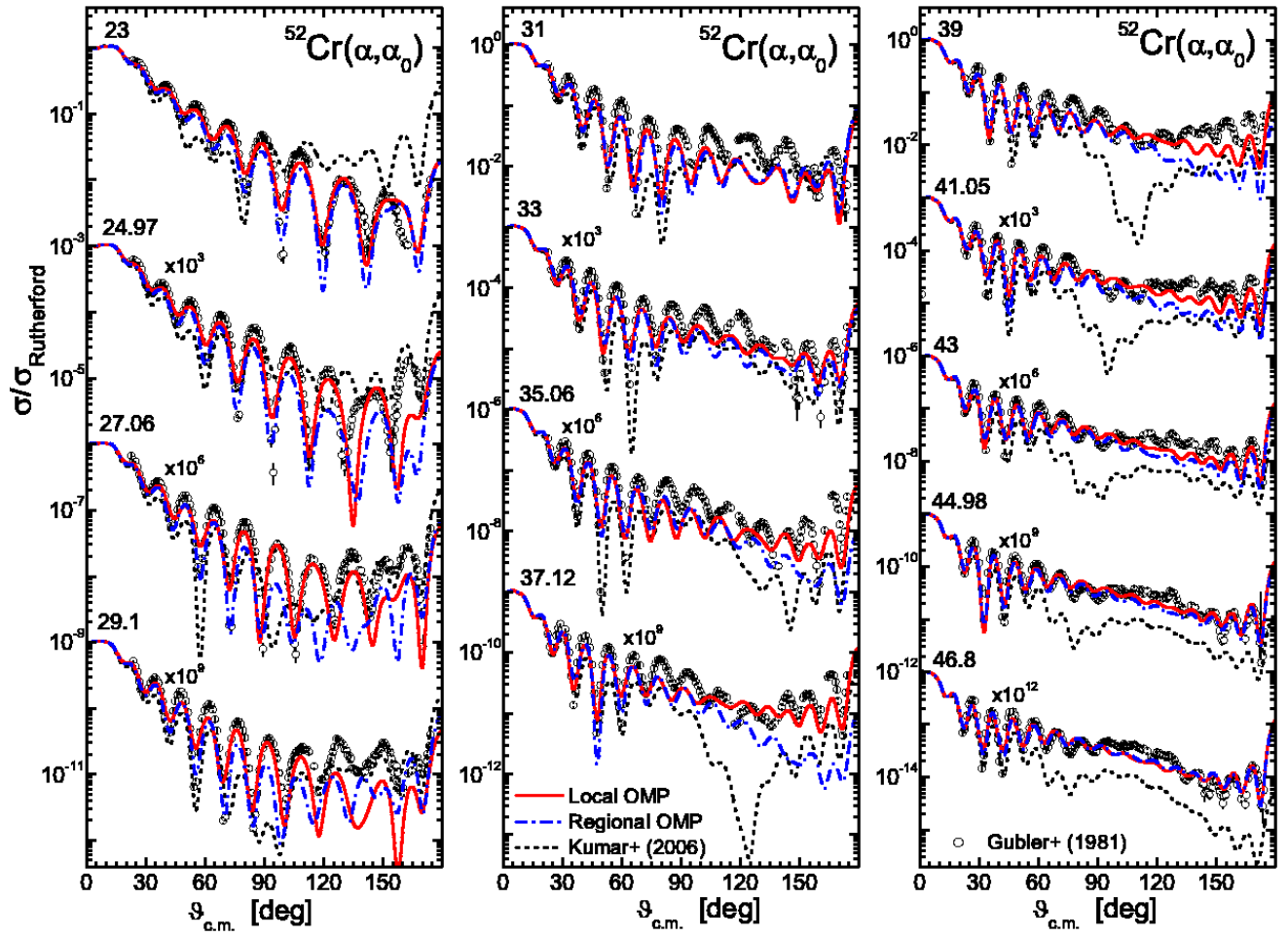


Fig. 3. (Color online) The same as in Fig. 1 but for α -particles scattered on ^{52}Cr between 23 and 47 MeV

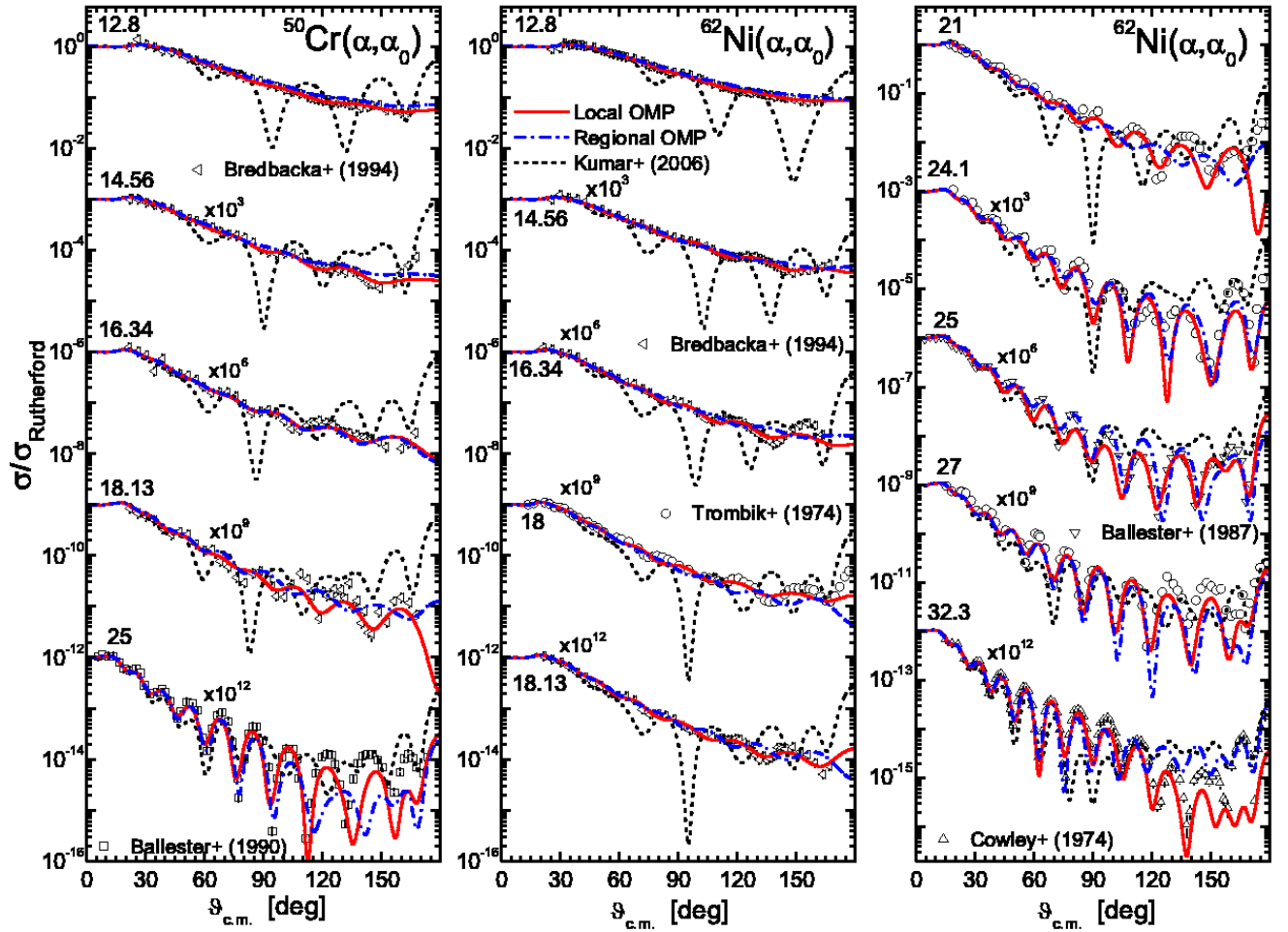


Fig. 4. (Color online) The same as in Fig. 1 but for α -particles scattered on ^{50}Cr between 13 and 25 MeV, and ^{62}Ni between 13 and 32 MeV.

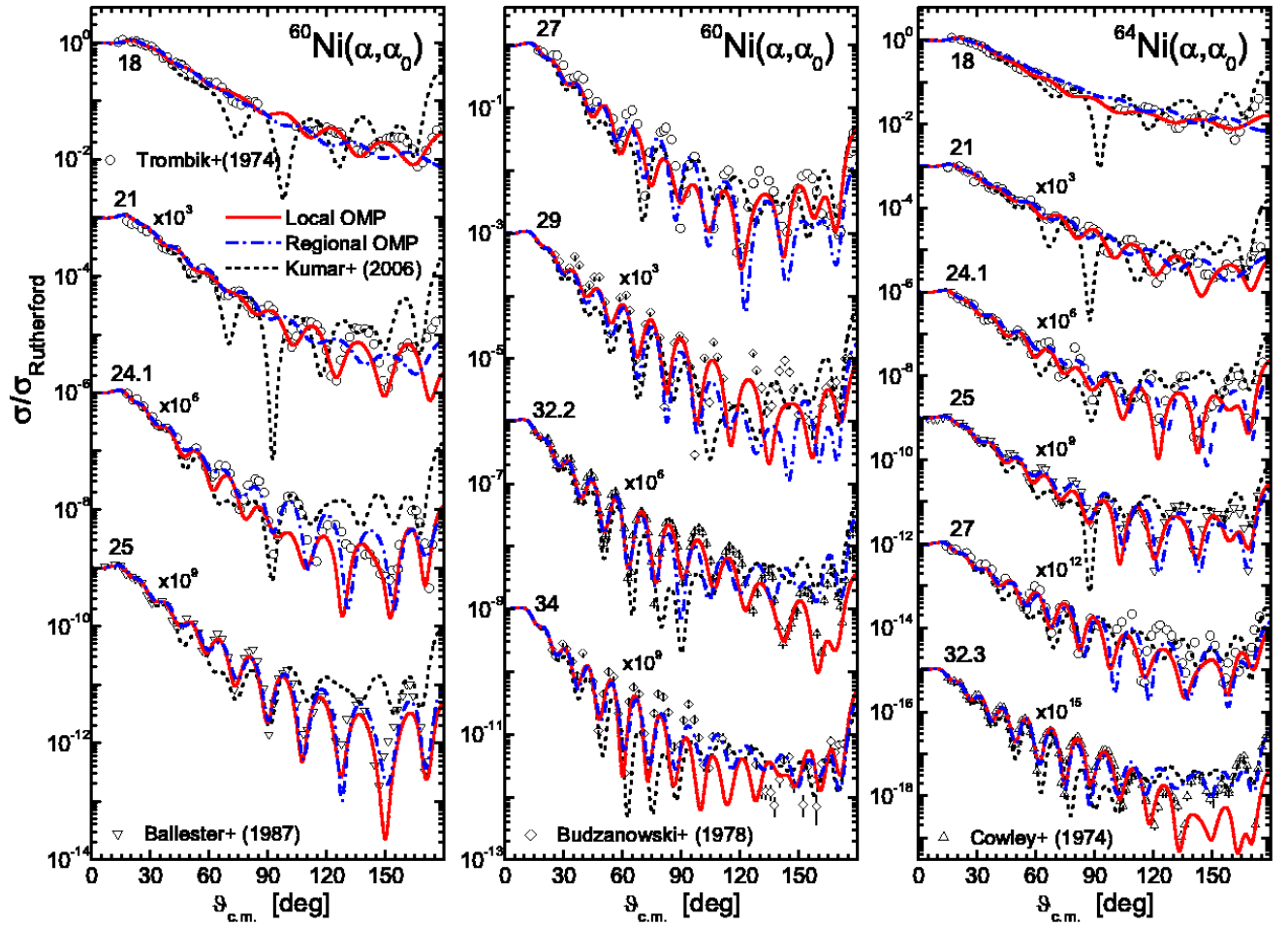


Fig. 5. (Color online) The same as in Fig. 1 but for α -particles scattered on ^{60}Ni between 18 and 34 MeV, and ^{64}Ni between 18 and 32 MeV.

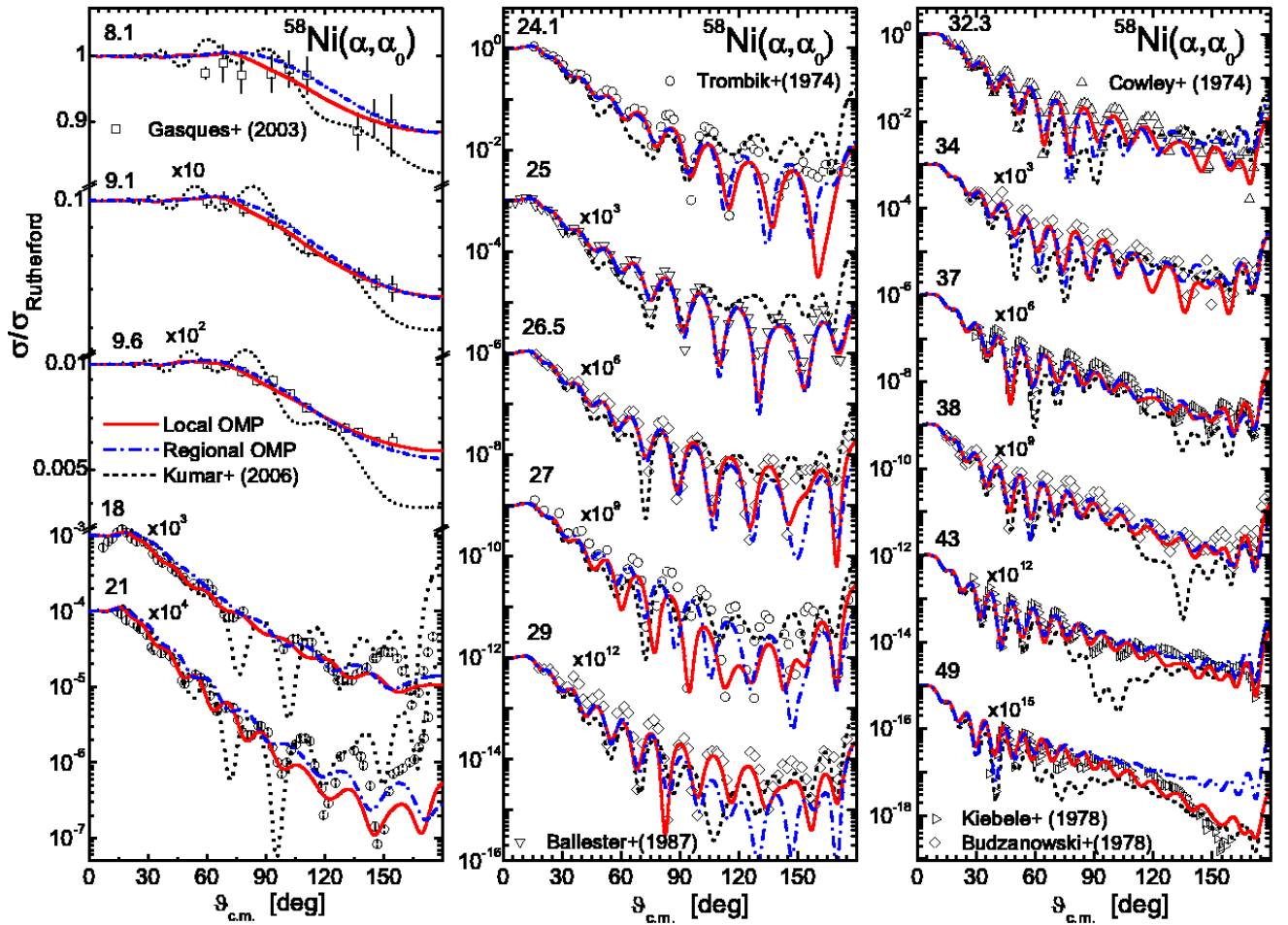


Fig. 6. (Color online) The same as in Fig. 1 but for α -particles scattered on ^{58}Ni between 8 and 49 MeV.

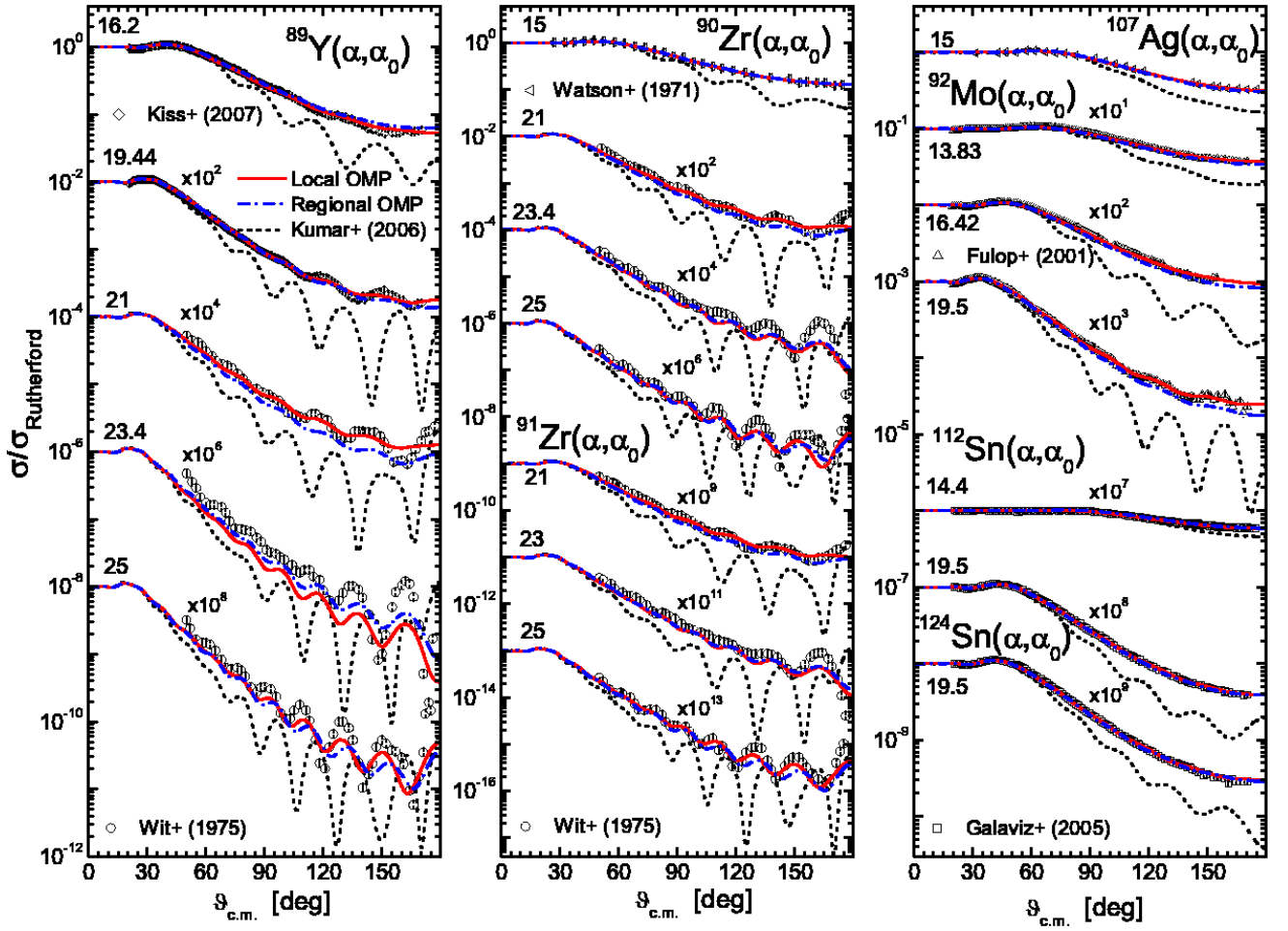


Fig. 7. (Color online) The same as in Fig. 1 but for α -particles scattered at 21, 23.4 and 25 MeV on ^{89}Y , $^{90,91}\text{Zr}$, ^{94}Mo , ^{107}Ag and $^{112,124}\text{Sn}$, between 14 and 25 MeV.

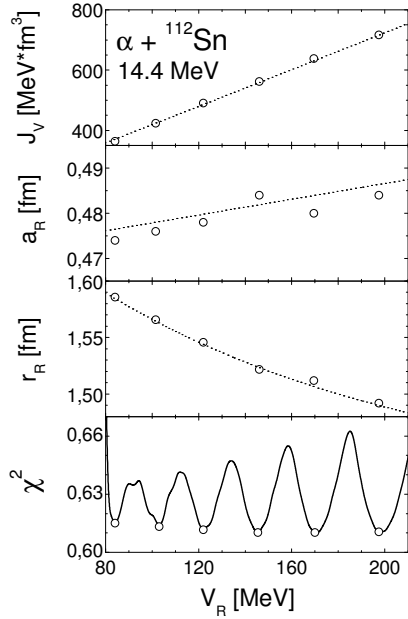


Fig. 8. The χ^2 deviation per degree of freedom between the experimental and calculated angular distributions of the elastic scattering of α -particles on ^{112}Sn at 14.4 MeV, versus the real potential depth V_R (solid curve), as well as the values of the real-potential radius r_R , diffuseness a_R and volume integral per interacting nucleon pair J_R , corresponding to the χ^2 minima. The dotted curves are drawn to guide the eye.

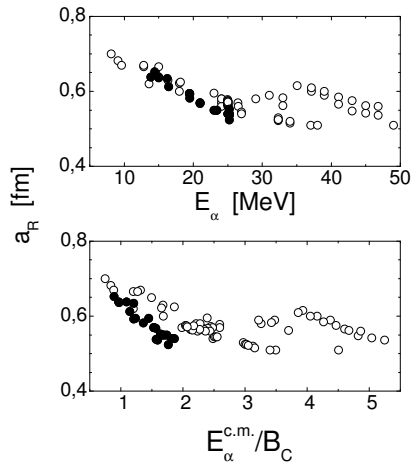


Fig. 9. The real-potential diffuseness a_R obtained by analysis of the experimental angular distributions of α -particle elastic scattering (Table 1) using the average values for the rest of all OMP parameters (Table 3), versus the α -particle energy (top) and its ratio in the center-of-mass system to the Coulomb barrier B_C (bottom). The full circles correspond to the target nuclei with $A > 89$.

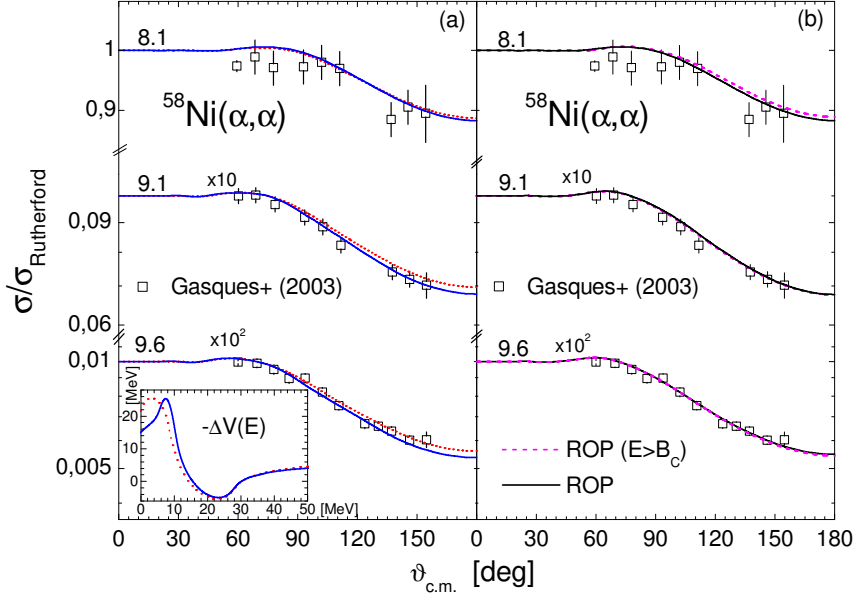


Fig. 10. (Color online) Comparison of measured [60] angular distributions of the elastic scattering of α -particles between 8.1 and 9.6 MeV on ^{58}Ni , with OMP calculations using (a) the local imaginary-potential parameters (Table 2) and semi-microscopic DF approach together with the surface-imaginary potential dispersive corrections formerly used within the elastic-scattering analysis (dotted curves) and corresponding to the final form of the ROP surface imaginary-potential in Table 3 (solid curves), and (b) the phenomenological parameters obtained formerly within the elastic-scattering analysis, i.e. for energies above the limit E_2 in Table 3 (dashed curves), and the final ROP (solid curves). In the inset of (a) are shown the same surface-imaginary potential dispersive corrections used for calculation of the angular distributions shown by the similar curves.

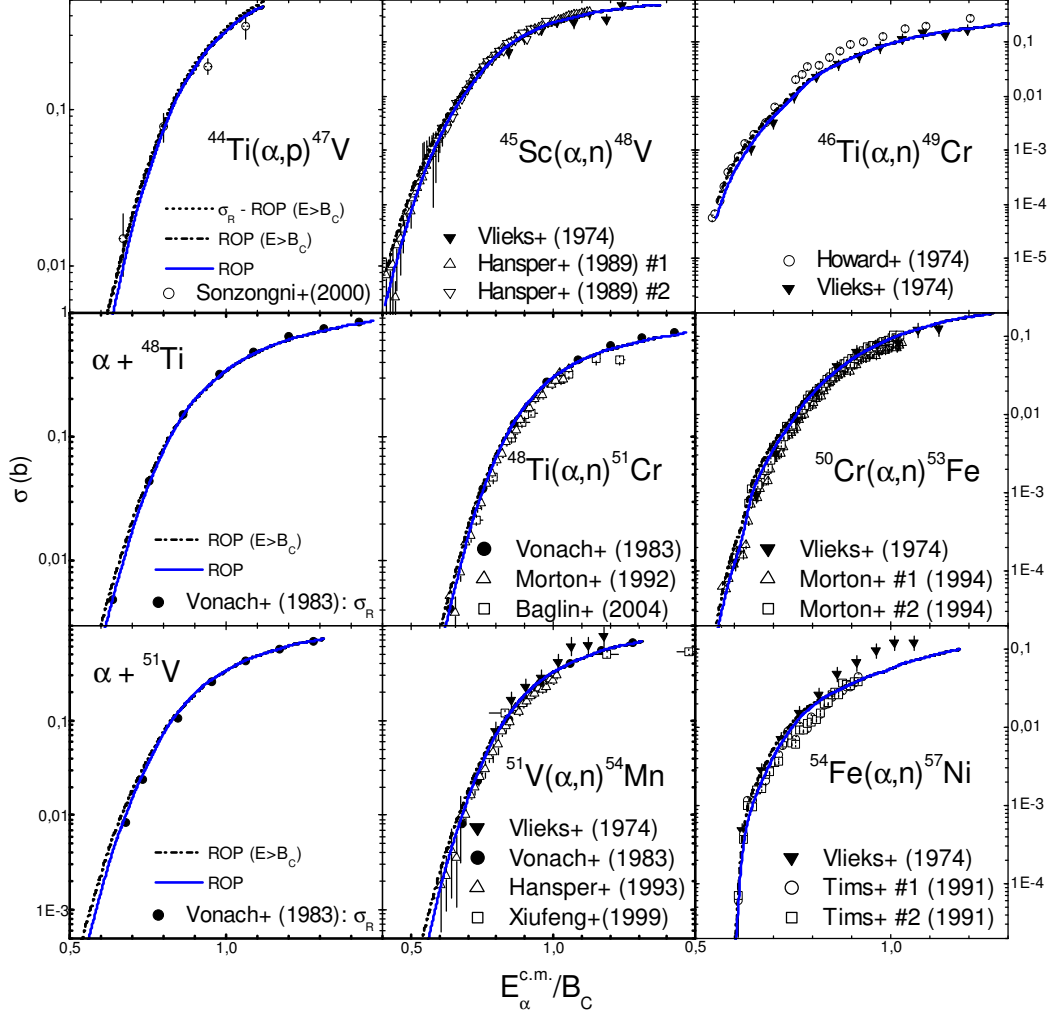


Fig. 11. Color online) Comparison of measured total α -reaction cross sections for ^{48}Ti and ^{51}V [28], and the related (α, n) reaction cross sections for ^{48}Ti [28,78,79] and ^{51}V [28,80,81,82], as well as for ^{45}Sc [80,83], ^{46}Ti [80,84], ^{50}Cr [80,85] and ^{54}Fe [80,86], and $^{44}\text{Ti}(\alpha,p)^{47}\text{V}$ reaction cross sections [87], with calculated values using the predictions of the present optical potential established by the elastic-scattering data analysis alone at energies above the Coulomb barrier B_C (dash-dotted curves) as well as its final form (Table 3) proved necessary for the (α, x) reaction data account (solid curves).

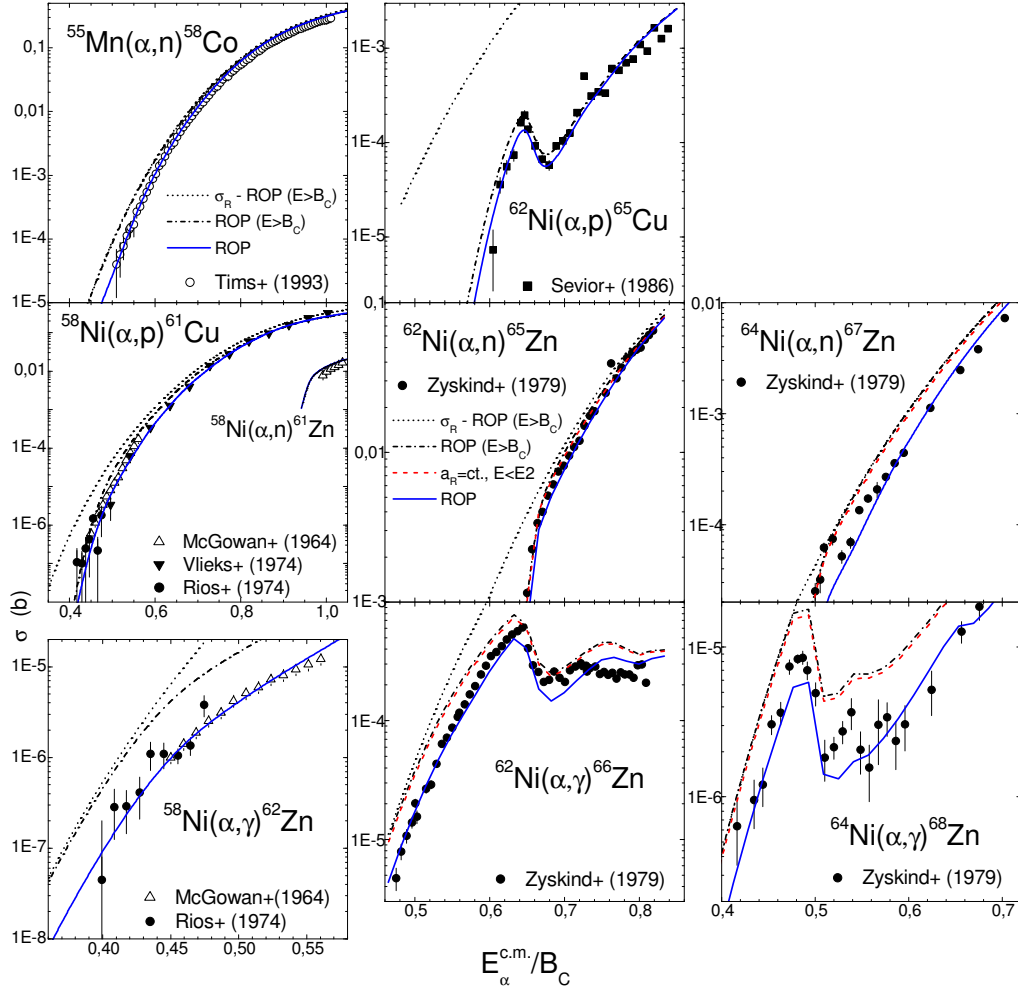


Fig. 12. (Color online) Comparison of measured (α, γ) , (α, n) and (α, p) reaction cross sections for ^{55}Mn [88], ^{58}Ni [80,89,90], ^{62}Ni [91,92], and ^{64}Ni [91] target nuclei, and calculated values using the predictions of the present optical potential established by the elastic-scattering data analysis alone at energies above the Coulomb barrier B_C (dash-dotted curves), as well as a constant real-potential diffuseness a_R at lowest energies below the energy E_2 given in Table 3 (dashed curves), and the final ROP proved necessary for the (α, x) reaction data account (solid curves). The total α -reaction cross sections provided at all energies by the ROP parameters established by the elastic-scattering analysis alone, are also shown (dotted curves) for a direct view of the weight of reactions being analyzed, by comparison with the corresponding dash-dotted curves.

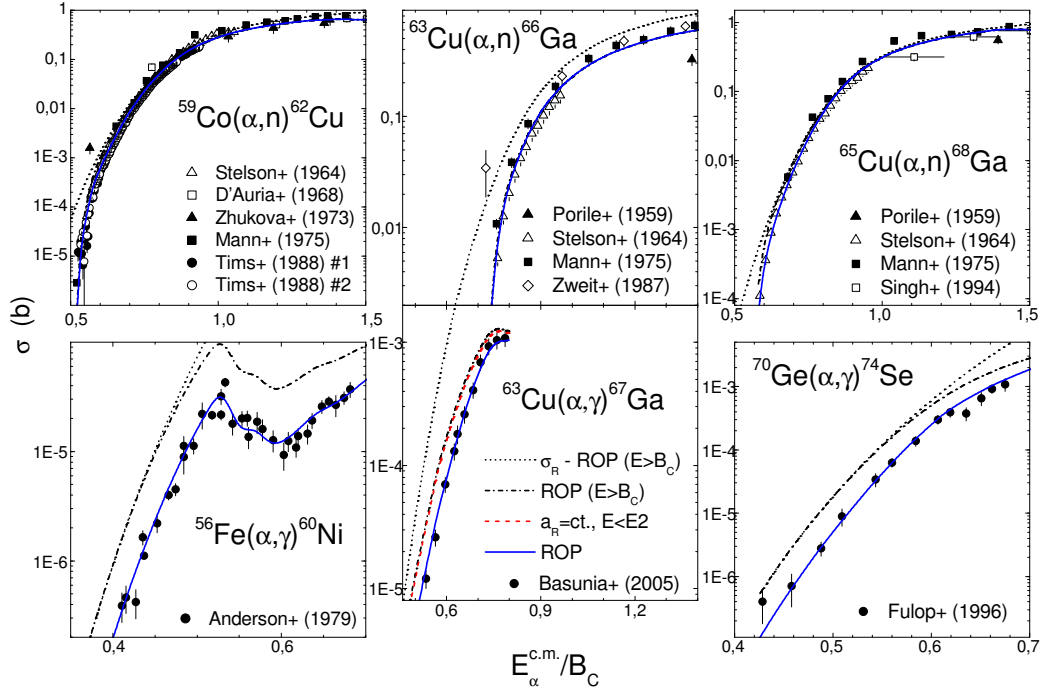


Fig. 13. (Color online) The same as in Fig. 12 but for the target nuclei ^{56}Fe [93], ^{59}Co [94,95,96,97,98], ^{63}Cu [20,94,97,99,100], ^{65}Cu [94,97,99,101], and ^{70}Ge [102].

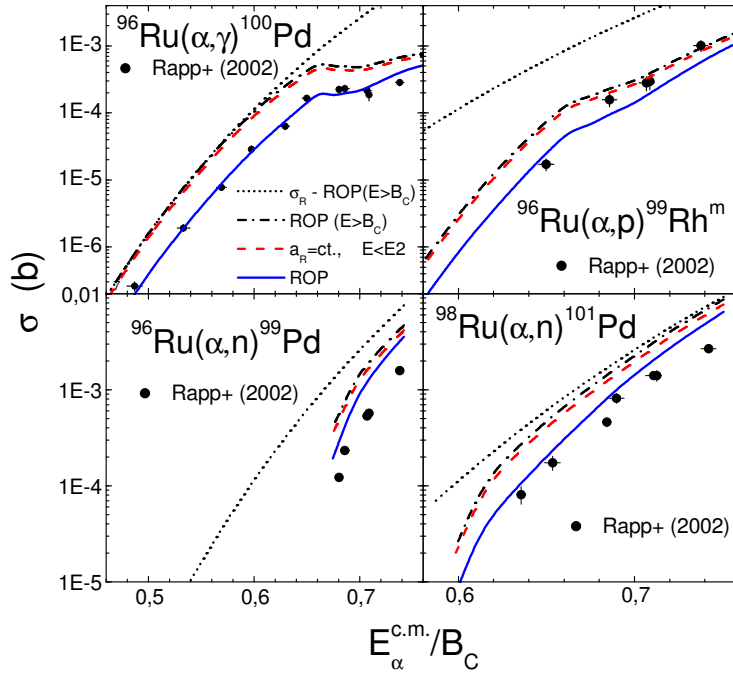


Fig. 14. (Color online) The same as in Fig. 12 but for the target nuclei $^{96,98}\text{Ru}$ [21].

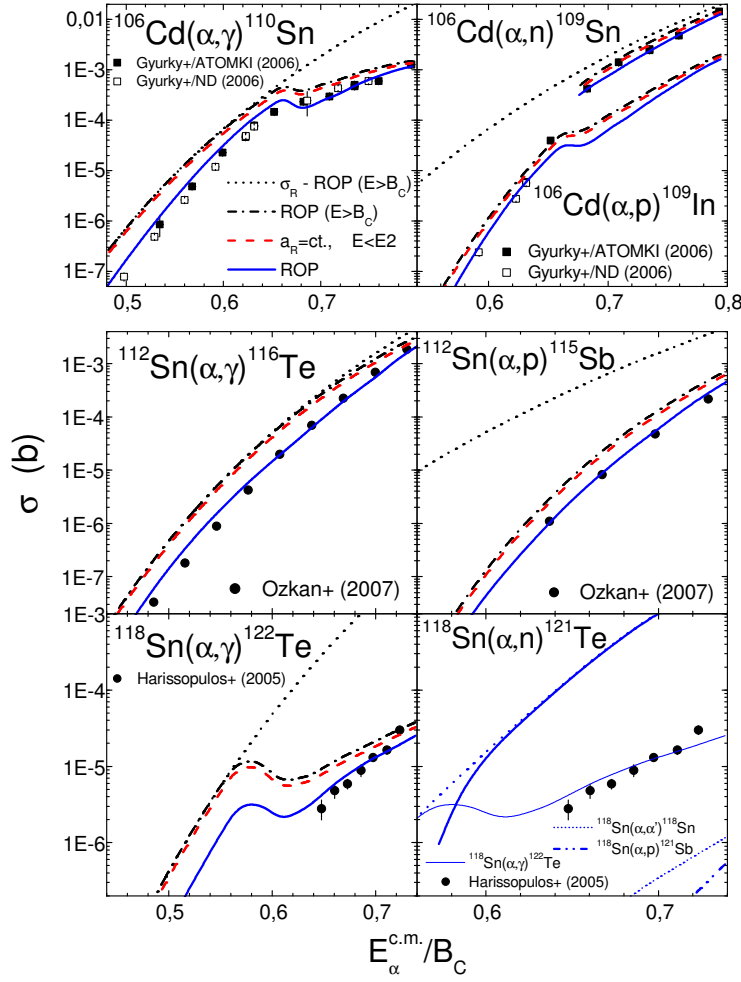


Fig. 15. (Color online) The same as in Fig. 12 but for the target nuclei ^{106}Cd [14] and $^{112,118}\text{Sn}$ [15,22], except the bottom-right corner where the final ROP proved necessary for the (α, x) reaction data account is used for all calculated cross sections of (α, n) (thick solid curve), (α, γ) (thin solid curve), (α, α') (short-dotted curve), and (α, p) (dash-dot-dotted curve) reactions.

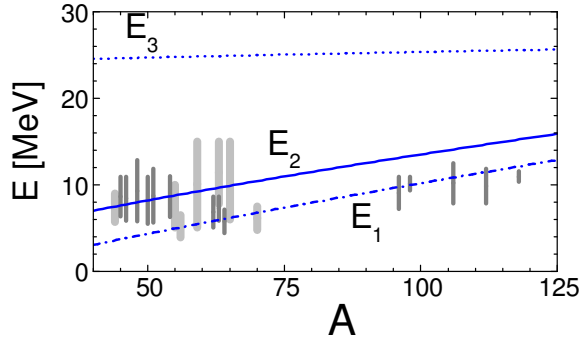


Fig. 16. (Color online) The energies E_1 (dash-dotted curve) below which the imaginary-potential depth $W_D=4$ MeV, E_2 (solid curve) corresponding to $0.9B_C$, and E_3 (dotted curve), at which the present ROP parameters change their energy dependences, versus the target nuclei atomic-mass number, and the energy ranges of the (α, x) reaction data formerly analyzed in the present work (thin vertical bars) as well as involved within the additional check of ROP (thick bars). The mass-dependences corresponding to nuclei with a nuclear asymmetry $(N-Z)/A$ value of 0.1 are shown, while the complete formulas of the energies E_1 , E_2 , E_3 are given in Table 3.